



THE UNIVERSITY *of* EDINBURGH

## Edinburgh Research Explorer

### Broken into Pieces:

**Citation for published version:**

Li, TS, Kuposov, SE, Erkal, D, Ji, AP, Shipp, N, Pace, AB, Hilmi, T, Kuehn, K, Lewis, GF, Mackey, D, Simpson, JD, Wan, Z, Zucker, DB, Bland-Hawthorn, J, Cullinane, LR, Costa, GSD, Drlica-Wagner, A, Hattori, K, Martell, SL & Sharma, S 2021, 'Broken into Pieces: ATLAS and Aliqa Uma as One Single Stream', *Astrophysical Journal*, vol. 911, no. 2, 149, pp. 1-24.

**Link:**

[Link to publication record in Edinburgh Research Explorer](#)

**Document Version:**

Early version, also known as pre-print

**Published In:**

*Astrophysical Journal*

**General rights**













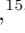







Copyright for the publications made accessible via the Edinburgh Research Explorer is retained by the author(s) and / or other copyright owners and it is a condition of accessing these publications that users recognise and abide by the legal requirements associated with these rights.

**Take down policy**

The University of Edinburgh has made every reasonable effort to ensure that Edinburgh Research Explorer content complies with UK legislation. If you believe that the public display of this file breaches copyright please contact [openaccess@ed.ac.uk](mailto:openaccess@ed.ac.uk) providing details, and we will remove access to the work immediately and investigate your claim.



## Broken into Pieces: ATLAS and Aliqa Uma as One Single Stream

TING S. LI <sup>1,2,\*</sup> SERGEY E. KOPOSOV <sup>3,4,5</sup> DENIS ERKAL <sup>6</sup> ALEXANDER P. JI <sup>1,†</sup> NORA SHIPP <sup>7,8,9</sup>  
ANDREW B. PACE <sup>3</sup> TARIQ HILMI <sup>6</sup> KYLER KUEHN <sup>10,11</sup> GERAINT F. LEWIS <sup>12</sup> DOUGAL MACKEY <sup>13</sup>  
JEFFREY D. SIMPSON <sup>14</sup> ZHEN WAN <sup>12,12</sup> DANIEL B. ZUCKER <sup>15,16</sup> JOSS BLAND-HAWTHORN <sup>12,17</sup>  
LARA R. CULLINANE <sup>13</sup> GARY S. DA COSTA <sup>13</sup> ALEX DRLICA-WAGNER <sup>9,7,8</sup> KOHEI HATTORI <sup>3</sup>  
SARAH L. MARTELL <sup>14,17</sup> AND SANJIB SHARMA <sup>12,17</sup>  
(*S*<sup>5</sup> COLLABORATION)

<sup>1</sup> *Observatories of the Carnegie Institution for Science, 813 Santa Barbara St., Pasadena, CA 91101, USA*

<sup>2</sup> *Department of Astrophysical Sciences, Princeton University, Princeton, NJ 08544, USA*

<sup>3</sup> *McWilliams Center for Cosmology, Carnegie Mellon University, 5000 Forbes Ave, Pittsburgh, PA 15213, USA*

<sup>4</sup> *Institute of Astronomy, University of Cambridge, Madingley Road, Cambridge CB3 0HA, UK*

<sup>5</sup> *Kavli Institute for Cosmology, University of Cambridge, Madingley Road, Cambridge CB3 0HA, UK*

<sup>6</sup> *Department of Physics, University of Surrey, Guildford GU2 7XH, UK*

<sup>7</sup> *Department of Astronomy & Astrophysics, University of Chicago, 5640 S Ellis Avenue, Chicago, IL 60637, USA*

<sup>8</sup> *Kavli Institute for Cosmological Physics, University of Chicago, Chicago, IL 60637, USA*

<sup>9</sup> *Fermi National Accelerator Laboratory, P.O. Box 500, Batavia, IL 60510, USA*

<sup>10</sup> *Lowell Observatory, 1400 W Mars Hill Rd, Flagstaff, AZ 86001, USA*

<sup>11</sup> *Australian Astronomical Optics, Faculty of Science and Engineering, Macquarie University, Macquarie Park, NSW 2113, Australia*

<sup>12</sup> *Sydney Institute for Astronomy, School of Physics, A28, The University of Sydney, NSW 2006, Australia*

<sup>13</sup> *Research School of Astronomy and Astrophysics, Australian National University, Canberra, ACT 2611, Australia*

<sup>14</sup> *School of Physics, UNSW, Sydney, NSW 2052, Australia*

<sup>15</sup> *Department of Physics & Astronomy, Macquarie University, Sydney, NSW 2109, Australia*

<sup>16</sup> *Macquarie University Research Centre for Astronomy, Astrophysics & Astrophotonics, Sydney, NSW 2109, Australia*

<sup>17</sup> *Centre of Excellence for All-Sky Astrophysics in Three Dimensions (ASTRO 3D), Australia*

### ABSTRACT

We present the first spectroscopic measurements of the ATLAS and Aliqa Uma streams from the Southern Stellar Stream Spectroscopic Survey (*S*<sup>5</sup>), in combination with the photometric data from the Dark Energy Survey and astrometric data from *Gaia*. From the coherence of spectroscopic members in radial velocity and proper motion, we find out that these two systems are physically one stream with discontinuity in morphology and density on the sky (the “kink” feature). We refer to this entire stream as ATLAS-Aliqa Uma stream, or AAU stream. We perform a comprehensive exploration of the effect of baryonic substructures and find that only an encounter with the Sagittarius dwarf  $\sim 0.5$  Gyr ago can create a feature similar to the observed “kink”. In addition, we also identify two gaps in the ATLAS component associated with the broadening in the stream width (the “broadening” feature). These gaps have likely been created by small mass perturbers, such as dark matter halos, as AAU stream is the most distant cold stream known with severe variations in both the stream surface density and the stream track on the sky. With the stream track, stream distance and kinematic information, we determine the orbit of the AAU stream and find that it has been affected by the Large Magellanic Cloud, resulting in a misalignment between the proper motion and stream track. Together with the Orphan-Chenab Stream, AAU is the second stream pair that has been found to be a single stream separated into two segments by external perturbation.

*Keywords:* stars: kinematics and dynamics; stars: abundances; Galaxy: kinematics and dynamics

## 1. INTRODUCTION

Testing the existence of low-mass ( $\lesssim 10^7 M_\odot$ ) dark matter subhalos places strong constraints on the particle nature of dark matter (e.g., Buckley & Peter 2018). In the currently preferred cosmological model of Lambda cold dark matter (CDM), structure formation is hierarchical. Dark matter clumps to form first smallest halos which then merge into massive ones (e.g., Springel et al. 2008). These dark matter halos are predicted to have subhalos, with subhalos hosting their own sub-subhalos down to the scale of the “minimum” mass set by the particle nature of dark matter. For example, calculations of the matter power spectrum associated with the popular CDM candidate “weakly interacting massive particle (WIMP) imply that the minimum mass of self-bound structures could be as small as an earth mass (Hofmann et al. 2001; Green et al. 2004; Diemand et al. 2005). Most alternative dark matter models behave like CDM on large scales, but produce different minimum dark matter halo masses. For example, warm dark matter (WDM) particle is less massive ( $m \sim \text{keV}$ ) than the CDM particle ( $m \gtrsim 10 \text{ GeV}$ ). The corresponding free-streaming scale of WDM erases fluctuations at the smallest scale and therefore the minimum halo mass becomes larger. The fuzzy dark matter model (e.g., Hu et al. 2000) posits an ultra-light dark matter particle ( $m \sim 10^{-22} \text{ eV}$ ) that the wave nature of dark matter particle becomes important, which prevents the formation of halos less massive than  $\sim 4 \times 10^7 M_\odot$  (Hui et al. 2017).

The lowest-mass dark matter halos are currently found through observations of the lowest *stellar* mass galaxies, which appear to live in  $10^{8-9} M_\odot$  halos (e.g., Koposov et al. 2009; Jethwa et al. 2018; Kim et al. 2018; Newton et al. 2018; Nadler et al. 2019, 2020). This matches theoretical expectations that baryonic effects like supernova feedback and reionization prevent star formation in halos below this scale (e.g., Bullock et al. 2001). Thus, one of the possible ways to probe dark matter halos at  $\lesssim 10^7 M_\odot$  is to observe the effects of star-free *dark subhalos* on matter with which they interact (e.g., Johnston et al. 2002). In a smooth gravitational potential, stellar streams formed by tidal disruption of globular clusters (e.g., Dehnen et al. 2004) would stretch into coherent mostly smooth bands on the sky (Küpper et al. 2010). However, a dark subhalo impacting the stream disturbs the smooth stream, forming gaps and wiggles

(e.g., Siegal-Gaskins & Valluri 2008; Yoon et al. 2011; Carlberg & Grillmair 2013; Erkal & Belokurov 2015a).

Dozens of thin, kinematically cold stellar streams have been discovered in the Milky Way halo (Grillmair & Carlin 2016; Shipp et al. 2018; Malhan et al. 2018; Ibata et al. 2019), and the most prominent ones have already been examined for evidence of density variations. Indeed, signatures consistent with  $10^6 M_\odot$  dark halo encounters have already been claimed in the Palomar 5 stream (e.g., Carlberg 2012; Erkal et al. 2017) and the GD-1 stream (e.g., Koposov et al. 2010; Carlberg & Grillmair 2013; Price-Whelan & Bonaca 2018; Bonaca et al. 2019b; de Boer et al. 2019). From these streams, the inferred abundance of dark matter subhalos down to  $\sim 10^6 M_\odot$  is consistent with the CDM predictions (e.g., Carlberg 2012; Banik & Bovy 2019). However, baryonic structures like giant molecular clouds (Amorisco et al. 2016; Banik & Bovy 2019), the Milky Way bar (Pearson et al. 2017; Erkal et al. 2017), spiral arms (Banik & Bovy 2019) and the disruption of the progenitor (Webb & Bovy 2019) can also produce stream perturbations that mimic the observational signature of dark subhalos. It is crucial to find more kinematically cold streams with perturbation signatures and better orbital constraints, which will improve our understanding of the baryonic effects on the streams as well as the impact of the smallest dark matter halos.

In this paper, we show that two recently discovered cold stellar streams – ATLAS and Aliqa Uma, which were previously thought to be unrelated – are in fact two components of a single system. The discontinuous on-sky morphology is caused by possible perturbations from either baryons or dark matter halos.

ATLAS was first discovered as a  $12^\circ$  long cold stellar stream (Koposov et al. 2014) in the first data release (DR1) of the VST ATLAS survey (Shanks et al. 2015). The detected length of the stream was mainly limited to the sky coverage of DR1. It was later analyzed by Bernard et al. (2016) using Pan-STARRS 1 (PS1) data (Chambers et al. 2016), which extended ATLAS to a total length of  $28^\circ$ . With the first three years of data from the Dark Energy Survey (DES; DES Collaboration 2016), Shipp et al. (2018) recovered  $22.6^\circ$  of the ATLAS stream within the DES footprint, at a heliocentric distance of 22.9 kpc.

Aliqa Uma was discovered in Shipp et al. (2018) in DES at a heliocentric distance of 28.8 kpc, residing at the southern end of the ATLAS stream. Despite the close proximity to the ATLAS stream, the difference in distance modulus and orientation on the sky led the au-

\* NHFP Einstein Fellow

† Hubble Fellow

thors to conclude that Aliqa Uma was a distinct stream, rather than an extension of ATLAS.

Both streams were observed by the Southern Stellar Stream Spectroscopic Survey ( $S^5$ ; Li et al. 2019, hereafter Paper I), which so far has provided 6D phase space information for 12 streams in the Southern Hemisphere with observations taken in 2018 and 2019, by combining AAT/AAOmega spectra with proper motions from *Gaia* DR2 (Gaia Collaboration et al. 2018a) and photometry from DES DR1 (DES Collaboration et al. 2018). As shown in Figure 12 of Paper I and reproduced in Figure 1 here, the high priority stream targets (proper motion selected metal-poor candidate members) in  $S^5$  show a clear connection in the line-of-sight velocities for these two streams. Similarly, Shipp et al. (2019) show that the proper motions of the two streams point in nearly the same direction (see Figure 5 in that paper). The kinematic information for the stream members suggests that these two streams are essentially one stream. In this paper, we confirm this hypothesis with kinematics, distances, and metallicities of the stream members, and further explore the physical origins of the discontinuity of the stream track on the sky.

The structure of the paper is as follows. We present the spectroscopic data from  $S^5$  in Section 2. We then revisit the stream with *Gaia* DR2 and other deep photometric data including DES DR1 in Section 3. We model the orbital motion of the stream in Section 4. We then discuss different properties of the streams in Section 5 and conclude in Section 6.

Throughout the paper, we use the rotation matrix for the ATLAS stream defined in Shipp et al. (2019), also shown in Appendix A, for converting celestial equatorial coordinates  $(\alpha, \delta)$  to stream coordinates  $(\phi_1, \phi_2)$ . We use  $(U_\odot, W_\odot) = (11.1, 7.3) \text{ km s}^{-1}$  (Schönrich et al. 2010) and  $V_\odot = \Omega_\odot R_\odot = 245 \text{ km s}^{-1}$  (Reid & Brunthaler 2004; Gravity Collaboration et al. 2019) to convert heliocentric velocity ( $v_{\text{hel}}$ ) to velocity in the Galactic standard of rest ( $v_{\text{GSR}}$ ). Unless otherwise noted, our  $gri$  magnitudes are reddening corrected photometry from DES DR1, specifically, taking the `WAVG_MAG_PSF` quantity corrected with  $E(B - V)$  from Schlegel et al. (1998) and the extinction coefficients from DES DR1.

All paper related materials including data, models and code used in this paper are publically available via GitHub repository.<sup>1</sup>

## 2. SPECTROSCOPIC DATA

### 2.1. $S^5$ Observations

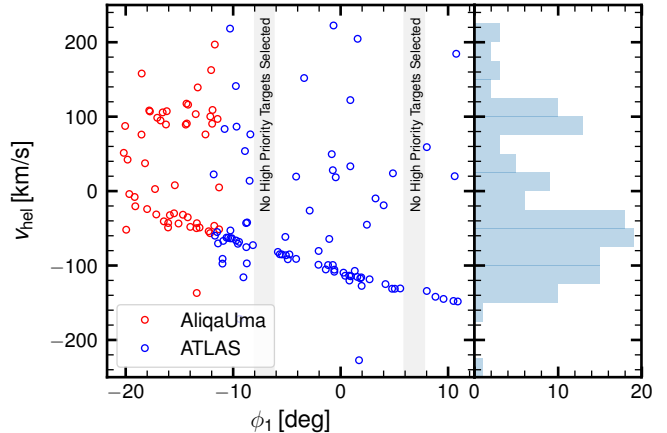


**Figure 1.** Heliocentric velocity as a function of stream longitude  $\phi_1$  for the high-priority targets with  $\log g < 4.1$  and  $[\text{Fe}/\text{H}] < -1$  in the fields of Aliqa Uma (red) and ATLAS (blue) streams. The grey bands show the fields that were observed prior to  $S^5$  (Field 8 and 15 in Figure 2) and therefore no high-priority targets were defined. These do not present any true gap in the member star distribution. The clear spectroscopic members of Aliqa Uma and ATLAS streams follow a coherent velocity trend from  $v_{\text{hel}} \sim -20 \text{ km s}^{-1}$  at  $\phi_1 \sim -20^\circ$  to  $v_{\text{hel}} \sim -140 \text{ km s}^{-1}$  at  $\phi_1 \sim +10^\circ$ . We also see additional kinematic substructure in the velocity distribution around  $v_{\text{hel}} \sim +100 \text{ km s}^{-1}$ , mostly in the Aliqa Uma stream field (also seen in the histogram in the right panel). We discuss this distinct substructure in Section 5.5.

The ATLAS and Aliqa Uma streams were observed in 2018 as part of the  $S^5$  program, which uses the AAOmega spectrograph on the 3.9 m Anglo-Australian Telescope (AAT), fed by the Two Degree Field (“2dF”) fiber positioner facility, allowing the acquisition of up to 392 simultaneous spectra of objects within a  $2^\circ$  field in diameter on the sky. We refer readers to Paper I for details on the survey strategy, target selection, observation and reduction of  $S^5$ . We briefly describe the observations and reductions for the two streams here.

A total of 5 AAT fields were observed in Aliqa Uma and 12 fields in ATLAS, with a total covered length of the stream of about  $34^\circ$  on the sky. Center of each field was separated by  $\sim 2^\circ$ . The top panel of Figure 2 shows the 17 AAT fields in ATLAS stream coordinates, denoted as Field 1 to 17. The Aliqa Uma stream is located at  $\phi_1 < -9^\circ$  (Field 1-5). As discussed in Paper I, the track of ATLAS is curved on the sky, and therefore we adopted the polynomial stream track from Shipp et al. (2018) for the ATLAS stream pointings. Two of the ATLAS fields (Field 8 and 15, encircled in red in the top panel of Figure 2) were observed prior to  $S^5$  as a pilot program, and therefore the target selection strategy, as well as the pointing strategy described in Paper I does

<sup>1</sup> [https://github.com/s5collab/ATLAS\\_AliqaUma](https://github.com/s5collab/ATLAS_AliqaUma)

not apply to these two fields. In particular, the selection for those two fields was performed without parallax and proper motion information from *Gaia* DR2. We aligned the rest of ATLAS fields to Field 15, but Field 8 is slightly misaligned, causing a small observational gap in  $\phi_1$  coverage around  $\phi_1 = -8^\circ$ .

The stream targets are selected using photometry from DES DR1 and astrometry from *Gaia* DR2. All the targets have been assigned a priority from P9 to P1, with P9 indicating the highest priority. While  $S^5$  included non-stream targets in the observation, stream targets usually have the highest priority in fiber assignment (P9-P7). The stream targets are selected as either red giant branch stars (RGBs) or blue horizontal branch stars (BHBs) based on their location on the dereddened color-magnitude diagram from DES DR1 photometry. The stream candidates are also selected to have proper motions consistent with measurements in Shipp et al. (2019). In addition, we put the metal-poor stream member candidates in the highest priority category (P9) based on color-color selection in a  $g - r$  vs.  $r - i$  diagram (see details in Paper I and Li et al. 2018). After all the stream targets are allocated, we use the spare fibers for additional targets in the field, such as RR Lyrae stars, hot stars, extremely metal-poor candidates, and low-redshift galaxy candidates.

The observed data were first reduced and extracted using the `2dfdr` pipeline provided by AAO Data Central<sup>2</sup>. The radial velocity and stellar parameters for each star were then derived by fitting the interpolated synthetic templates from the PHOENIX spectral grid (Husser et al. 2013) modified by a polynomial continuum using the `RVSPECFIT` code (Koposov et al. 2011; Koposov 2019). The means and uncertainties of the radial velocity and stellar parameters are derived from the posterior distribution samples obtained from a Markov Chain Monte Carlo (MCMC) sampler. For stars with multiple observations, the measurements with highest S/N are used.

## 2.2. Spectroscopic Member Identification

We use the radial velocities (RVs) from  $S^5$  and proper motions (PMs) from *Gaia* DR2 to determine the spectroscopic members in these two streams. Meanwhile, we find the best track in RV and PM space as a function of the stream longitude,  $\phi_1$ , that defines the selection criteria of the spectroscopic members.

We first select stars with `good_star` = 1 (see definition in Paper I) to ensure the quality of spectral template fit

and the derived radial velocities. In addition, we only consider stars with parallax ( $\omega$ )

$$\omega < \max(3\sigma_\omega, 0.1)$$

to exclude any nearby disk stars. We then selected the spectroscopic members through an iterative process following three steps:

1. We fit a 2<sup>nd</sup>-order polynomial function to  $v_{\text{GSR}}$ ,  $\mu_\alpha \cos \delta$  and  $\mu_\delta$  for the spectroscopic members to define the kinematic track of the stream. To start the first round polynomial fit, we selected an initial sample from the high priority targets with  $-140 < v_{\text{GSR}}/\text{km s}^{-1} < -120$ . We also ignore all the RR Lyrae member stars in fitting  $v_{\text{GSR}}$  as their line-of-sight velocities vary from their true systemic velocity due to pulsation.

2. We select spectroscopic members that are within  $\pm 0.55 \text{ mas yr}^{-1}$  in  $\mu_\alpha \cos \delta$  and  $\mu_\delta$  and  $\pm 25 \text{ km s}^{-1}$  in  $v_{\text{GSR}}$  from the best-fit track.

3. We visually inspect the spectra and the best-fit templates for these selected spectroscopic members, and we discard any members with unreliable radial velocity measurements. We note that the cut on `good_star` = 1 discarded most spectra with bad template fits, and we found that < 5% of the selected stars did not pass our visual inspection.

We then repeat the above procedures iteratively until there are no changes in the final spectroscopic sample. A total of 96 spectroscopic members are identified kinematically (71 in ATLAS and 25 in Aliqa Uma, presented in Table 1), along with the best fit track in radial velocity and in proper motion defined as:

$$\begin{aligned} \text{Track}_{rv}(\text{km s}^{-1}) : \quad & v_{\text{GSR}} = -131.33 + 0.07x + 5.68x^2 \\ \text{Track}_{\mu,\alpha}(\text{mas yr}^{-1}) : \quad & \mu_\alpha \cos \delta = -0.10 - 0.34x - 0.09x^2 \\ \text{Track}_{\mu,\delta}(\text{mas yr}^{-1}) : \quad & \mu_\delta = -0.96 - 0.07x + 0.07x^2 \end{aligned} \quad (1)$$

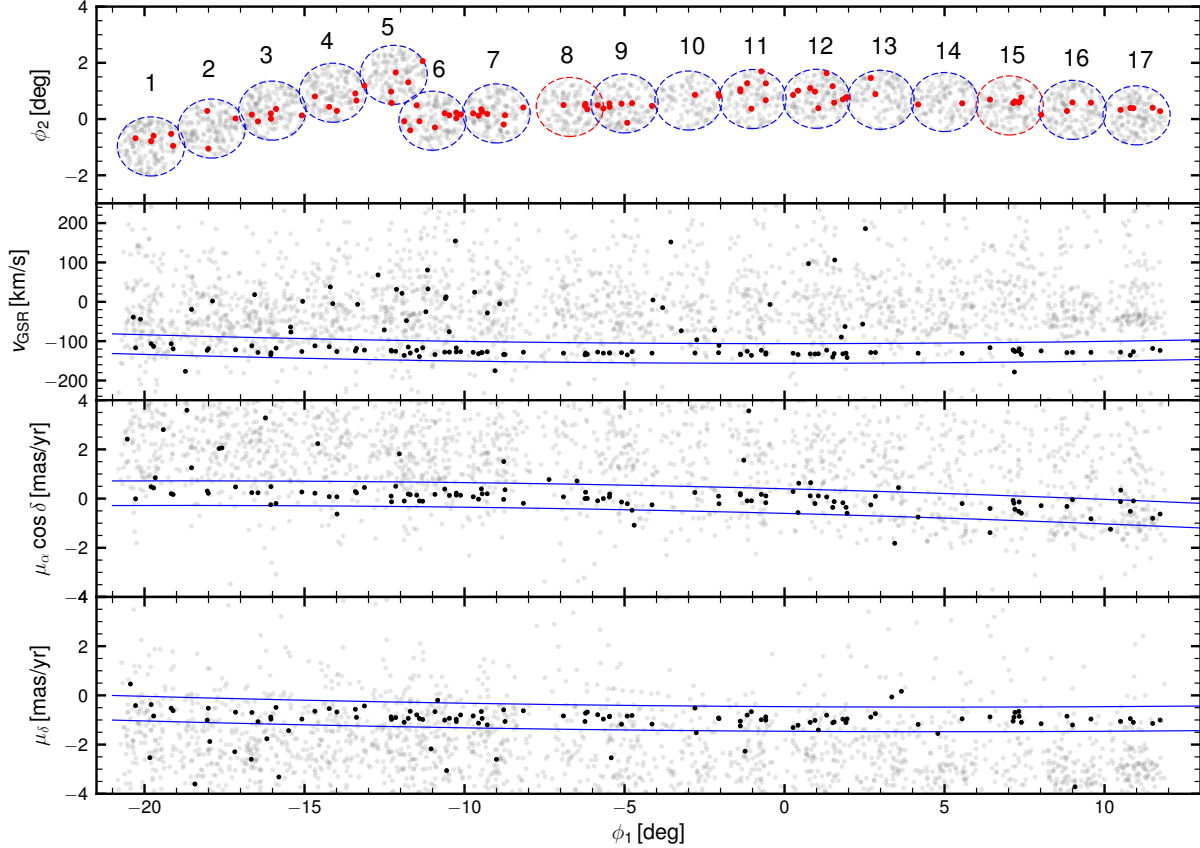
where  $x = \phi_1/10^\circ$ , with  $\phi_1$  measured in degrees.

Figure 2 shows the spectroscopic members selected with the best-fit track. In the top panel, red filled circles indicate the final spectroscopic members selected with all three components (radial velocity and two proper motions). In each of the bottom three panels, the black dots show the candidate members selected with only the other two components, i.e. black points in the bottom ( $\mu_\delta$ ) panel were selected using the track in radial velocity and  $\mu_\alpha \cos \delta$  only. The panels clearly show a group of likely stream members predominantly occupying the region next to the best fit track enclosed in solid blue lines.

In Figure 3, we show the distance to the best-fit track for each star in RV and PM space. We note that our se-

<sup>2</sup> <https://www.aao.gov.au/science/software/2dfdr>





**Figure 2.** Selection of spectroscopic members based on radial velocity ( $v_{\text{GSR}}$ ) and proper motions ( $\mu_{\alpha} \cos \delta$  and  $\mu_{\delta}$ ) of the observed stars. In all panels, grey points show all stars observed by  $S^5$ . The top panel shows the location of 17 AAT fields in stream-aligned coordinates observed in 2018; two of them (encircled in dashed red) were observed prior to  $S^5$  as part of a pilot program. The red filled circles show the 96 spectroscopic members selected with the best fit track in RV and PM (blue solid lines in other three panels). The bottom three panels show the kinematic distribution of the spectroscopic sample. In all three panels, black dots show the spectroscopic sample passing the selection criteria in other two components (i.e. in between the blue lines in the other two panels). The blue lines are defined as the best fit track (see text for details) plus the width (i.e.  $\pm 25 \text{ km s}^{-1}$  in  $v_{\text{GSR}}$  and  $\pm 0.55 \text{ mas yr}^{-1}$  in both  $\mu_{\alpha} \cos \delta$  and  $\mu_{\delta}$ ). See Figure 5 for a zoomed in version of this plot for member stars only.

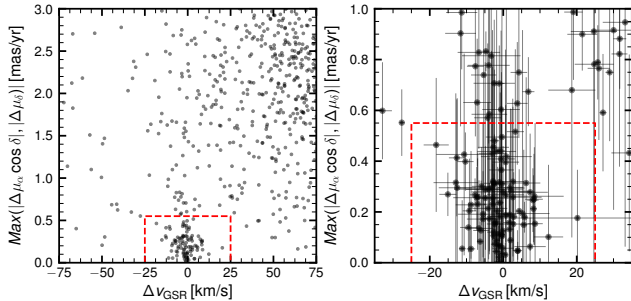


**Figure 3.** (left) The distance to the best fit track in RV and PM. For PM, the larger distance in either  $\mu_{\alpha} \cos \delta$  or  $\mu_{\delta}$  is shown. The red dashed lines show the selection width of the spectroscopic members, and stars in the red box are considered as spectroscopic members in this paper. (right) Zoomed-in version of the left panel with uncertainties shown.

lection window is quite narrow with respect to the uncer-

tainties, especially in proper motion ( $\pm 0.55 \text{ mas yr}^{-1}$ ). This is to ensure a clean sample for further investigation in the rest of this paper. Our selection will inevitably miss some members with large proper motion uncertainties at fainter magnitude. However, these missed member stars likely have larger measurement uncertainties, so their absence does not significantly affect the measurements of the radial velocity and proper motion tracks.

A color-magnitude diagram (CMD) of the 96 kinematically identified spectroscopic members is shown in the left panel of Figure 4. With the kinematic selection described above, we found a total of 13 blue horizontal branch (BHB) member stars at  $-0.3 < (g-r)_0 < 0.0$ . In addition, five members are classified as RR Lyrae stars (RRLs) in *Gaia* DR2. The majority of members are red-giant branch (RGB) stars. We note that most

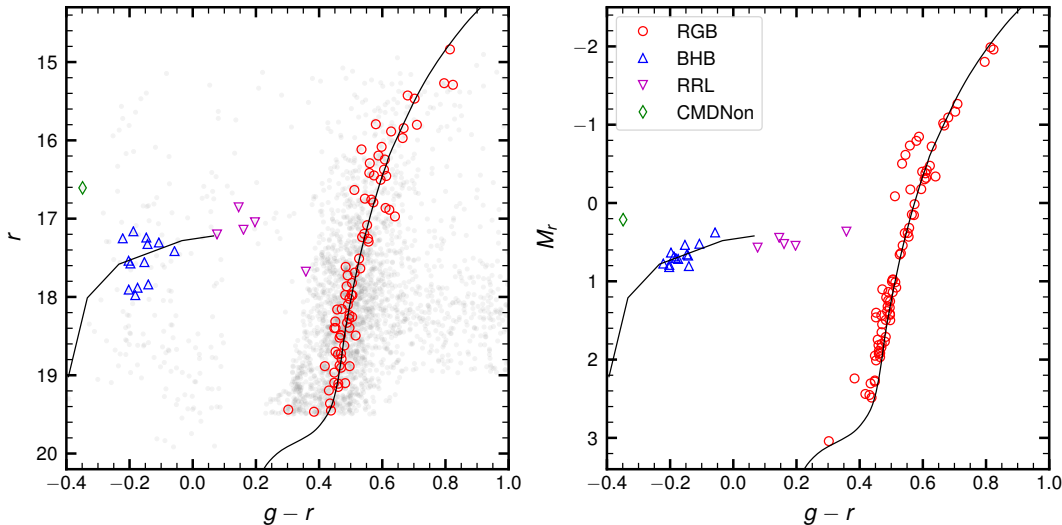


**Figure 4.** (left) Color-magnitude diagram of the spectroscopic stream members. While the member stars are selected kinematically (i.e. Figure 2), most of them can be well described by a stellar isochrone at distance modulus  $m - M = 16.8$ . The BHB isochrone is taken from the globular cluster M92 (Clem 2006; Belokurov et al. 2007) and the RGB isochrone is taken from the Dartmouth Stellar Evolution Database (Dotter et al. 2008) with parameters detailed in Section 3.1. Grey dots show all the stars observed in the 17 AAT fields and different symbols show member stars in different stellar populations, including red giant branch (RGB) stars, blue horizontal branch (BHB) stars, and RR Lyraes (RRL). We also note one CMD non-member (CMDNon), which has kinematic properties consistent with being a member star. (right) HR diagram of the same spectroscopic members corrected for the  $\phi_1$  dependent distance as measured in Section 2.3. With distance correction, both the horizontal branch sequence and red giant branch sequence become significantly tighter. A group of Asymptotic Giant Branch (AGB) stars also become visible at  $M_r \sim -0.75$ .

of the kinematically selected members are well aligned with the stellar isochrone shown as the black curves. The only exception is a blue star at  $(g - r)_0 \sim -0.35$  and  $r_0 \sim 16.6$ . This star deviates from the other BHBs in CMD and is marked by a green diamond. It is a CMD non-member star; however, it is kinematically consistent with other stream members (see Figure 5;  $\phi_1 \sim 12^\circ$ ).

We now have a closer look at the spectroscopic members in Figure 5. These 96 members are coded with different symbols by their stellar populations defined in Figure 4. We highlight that although a  $\Delta v_{\text{GSR}}$  of  $25 \text{ km s}^{-1}$  is used for the spectroscopic member selection (dashed line in the second panel), most of the members are very close to the RV track (black line), further confirming our robust identification of the spectroscopic members. Despite the spatial discontinuity around  $\phi_1 \sim -12^\circ$  (Field 5 and 6), the line-of-sight velocities and proper motions of the two streams are seamlessly connected, strongly confirming that these two are indeed one single stream. For the remainder of the paper, we will refer the entire stream as the ATLAS-Aliqa Uma stream, or the AAU stream. We refer to the discontinuity feature as a “kink” in the rest of the paper. Furthermore, when looking at top panel of Figure 5, we found that the stream also displays a broader width at  $-2^\circ < \phi_1 < 2^\circ$  (Field 11 and 12). Such broadening in

stream width might be associated with a density variation in the stream and we investigate this further via deeper photometry in Section 3. We refer to this feature as a “broadening” hereafter.

### 2.3. Distance Gradient from BHB and RRL

In addition to the discontinuity of the two streams on the stellar density map, Shipp et al. (2018) did not associate these two streams because their distance moduli are different by 0.5 magnitude (i.e.  $m - M = 16.8$  for ATLAS and 17.3 for Aliqa Uma). Therefore, the kinematic connection between these two streams suggests there should also be a distance gradient along these two streams. Luckily, both spectroscopically confirmed BHBs and RRLs are good distance indicators for such a study. As shown in Figure 6, BHB and RRL members are well populated along the stream. We first derive the distance modulus of each BHB member star  $m - M = g - M_g$  using the  $M_g$  vs  $(g - r)$  relation from Belokurov & Koposov (2016). Assuming the uncertainty on distance modulus for each BHB is 0.1 mag (Deason et al. 2011), we fit the distance modulus with a second order polynomial:

$$\text{Track}_{dm} : (m - M) = 16.66 - 0.28x + 0.045x^2 \quad (2)$$

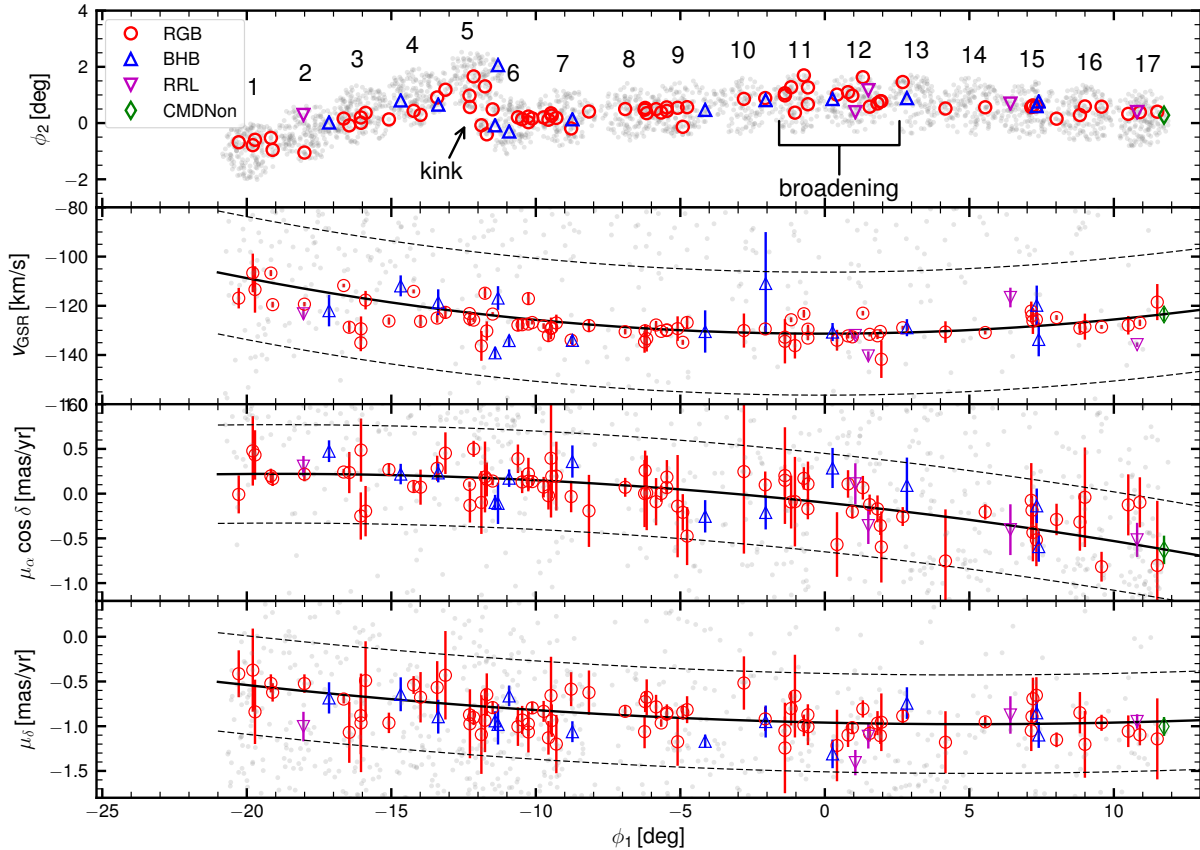


**Figure 5.** Zoom-in of Figure 2 with spectroscopic members with the same symbols as in Figure 4. The vertical bar in each symbol shows the uncertainties of the RV or PM measurements (many stars have RV uncertainties smaller than the size of the symbol). In the bottom three panels, the solid line shows the best-fit tracks (Eqn. 1-3) and the dashed lines show the width of the spectroscopic member selection (i.e. red dashed lines in Figure 3.)

where  $x = \phi_1/10^\circ$ . We emphasize that this relation is derived using BHBs between  $\phi_1 \sim -17^\circ$  and  $\phi_1 \sim 7^\circ$ . Extrapolation on the distance beyond these two points should be done with caution. In both panels, one BHB star around  $\phi_1 \sim -11.5^\circ$  that is circled in cyan has a distance modulus that is 0.3 magnitudes larger than the other two BHB stars at similar  $\phi_1$ . This may be an indication that at the location of the “kink” there is a distance spread, and that the Aliqa Uma component of the stream is further than the ATLAS component. This also matches with the line-of-sight velocity variation in this area as discussed later in Section 2.4 and Figure 7.

We derived the distance using the RRL members as an independent check. To do that, we take the  $M_G - [\text{Fe}/\text{H}]$  relation from Muraveva et al. (2018), assuming a stellar metallicity of  $[\text{Fe}/\text{H}] = -2.2$  (see Section 2.5), and  $G$ -band magnitude from Gaia DR2 with color-dependent extinction corrections from Gaia Collaboration et al. (2018b) and the Schlegel et al. (1998) values of  $E(B - V)$ . The derived distance modulus for the confirmed RRL members are shown as magenta circles in Figure 6. Four of the five spectroscopic RRL members

have distances consistent with those of BHB members, and the one exception is the RRL at  $\phi_1 \sim 6.5^\circ$ . We notice that this star only has 11 transits selected for variability analysis from Gaia DR2 (`num_selected_g_fov` = 11), while the other RRL members that have over 30 transits; this might lead to an imprecise distance estimation. In addition to the spectroscopically confirmed RRL members, we checked all RRLs at  $|\phi_2| < 2$  and  $16 < m - M < 18$  in Gaia DR2, shown as open green circles in Figure 6. While some of these RRLs are likely non-members of the streams, it is possible that two RRLs at  $\phi_1 \sim -6^\circ$  are members of ATLAS stream, as they are at the right distance<sup>3</sup>. Spectroscopic follow-up on these RRLs is necessary to confirm their membership.

#### 2.4. Line-of-sight Velocity Dispersion

<sup>3</sup> These two RRLs are not included in the spectroscopic observations as Field 8 was observed prior to  $S^5$ , so RRL candidates were not part of the target selection.



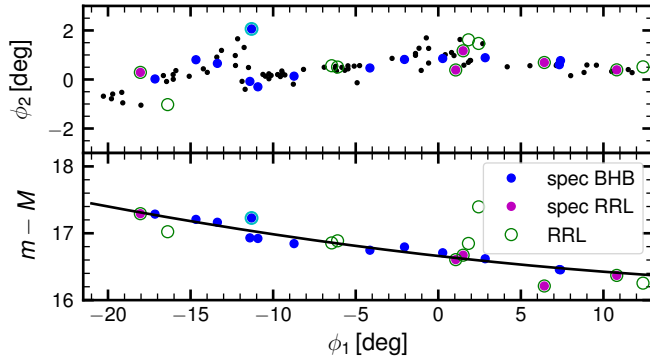


**Figure 6.** On sky distribution (top) and heliocentric distances (bottom) of BHBs and RRLs in the area of the streams. A 2<sup>nd</sup> order polynomial fit on distance modulus ( $m - M$ ) of the BHBs is shown as black curve. In all panels, we also show all RRLs in the stream area with  $16 < m - M < 18$  from *Gaia* DR2 as open circles. We note that likely not all of them are stream members. In both panels, a BHB star at  $\phi_1 \sim -11.5^\circ$  is encircled in cyan. This BHB shows a slightly greater distance ( $\Delta(m - M) \sim 0.3$ ) than the other two BHB stars in the ATLAS stream at a similar  $\phi_1$ . The difference is significantly larger than the distance uncertainty of BHB stars (at 0.1–0.2 mag) and may indicate a distance spread in this area.

A stream’s velocity dispersion is a useful indicator of the stream’s progenitor type and orbital interaction history. For example, the velocity dispersion of the Sagittarius dwarf galaxy stream is  $\sim 10 - 20 \text{ km s}^{-1}$  (Koposov et al. 2013; Gibbons et al. 2017) in contrast to the Palomar 5 globular cluster stream, which has a velocity dispersion of  $2.1 \pm 0.4 \text{ km s}^{-1}$  (Kuzma et al. 2015). However, streams are not in dynamical equilibrium, so the dispersion cannot be directly translated to a dynamical mass for the stream progenitor.

We study the velocity dispersion along the AAU stream using  $\Delta v_{\text{GSR}}$ , which is defined as the difference between  $v_{\text{GSR}}$  and the RV track.<sup>4</sup> We model the  $\Delta v_{\text{GSR}}$  with a Gaussian distribution while taking into account velocity uncertainties of individual stars. The posterior on the velocity dispersion was obtained by MCMC sampling, similar to what has been done in kinematic studies of ultra-faint dwarf galaxies (e.g. Walker et al. 2006; Li et al. 2017). We use a flat prior for mean velocity and logarithmic prior (i.e. flat prior in log-space) for the velocity dispersion. The velocity dispersion is measured to be  $4.8 \pm 0.4 \text{ km s}^{-1}$  for the entire stream.

We study the variation of the velocity dispersion along the stream in the left panel of Figure 7. In particu-

lar, we are interested in the velocity dispersion at the “kink” ( $\phi_1 \sim -12^\circ$ ) and at the “broadening” ( $\phi_1 \sim 0^\circ$ ). We therefore divided the stream into four portions and calculated the velocity dispersion of each portion. We found that, even with the velocity uncertainty taken into account, the dispersions around those features are indeed larger than the rest of the stream. While the increase of the dispersion at the “broadening” is not significant, the dispersion for Aliqa Uma is significantly larger, suggesting a severe perturbation in the past.

From the top panel of Figure 7, it also seems that there is a correlation between the position of the star relative the stream track on the sky and the velocity offset w.r.t. the track, i.e.,  $\Delta v_{\text{GSR}}$ . This is especially obvious for stars at  $-12^\circ \lesssim \phi_1 \lesssim -11^\circ$ , where the streams connect. The right panel of Figure 7 shows a strong correlation between  $\Delta v_{\text{GSR}}$  and  $\phi_2$  based on the six members in this area, which might be an imprint from an earlier perturbation. More RV measurements for stars in the connecting region between the two streams are required to understand the origin of the perturbation.

### 2.5. Metallicities and Metallicity dispersion

As discussed in Paper I, although *rvspectfit* returns the stellar atmospheric parameters including metallicity of stars in  $S^5$ , metallicities derived from equivalent width of Calcium triplet (CaT) lines using the relation from Carrera et al. (2013) show better precision when comparing with the metallicities derived from high-resolution spectroscopy, for stars with known distances such as stream members. This empirical metallicity calibration relation only applies to RGB stars with known distance, because the absolute magnitudes of the stars are required for the empirical calibration. We therefore derived the CaT metallicities for the RGB member stars using the distance relation defined in Eqn 2.

The equivalent widths of the CaT lines are derived by fitting a Gaussian plus a Lorentzian function on three lines. For spectra with very low signal-to-noise ratio, the fit sometimes fails. We therefore select the RGB members with spectral S/N  $> 8$  per pixel and visually inspect the fitting quality on the equivalent widths for each individual spectrum. This results in 50 RGB members with reliable metallicity measurements which are presented in Table 1. The metallicities of these 50 RGBs are shown in the left panel of Figure 8. The metallicities of the two stream components appear quite similar. As stars in Aliqa Uma are slightly further away and therefore fainter, the stellar metallicities show larger scatter in smaller  $\phi_1$  with larger metallicity uncertainties.

We then derive the mean metallicity and metallicity dispersion of the AAU stream. In order to take into ac-

<sup>4</sup> RRL members are excluded in this analysis as the velocities of RRL stars varies with phase.

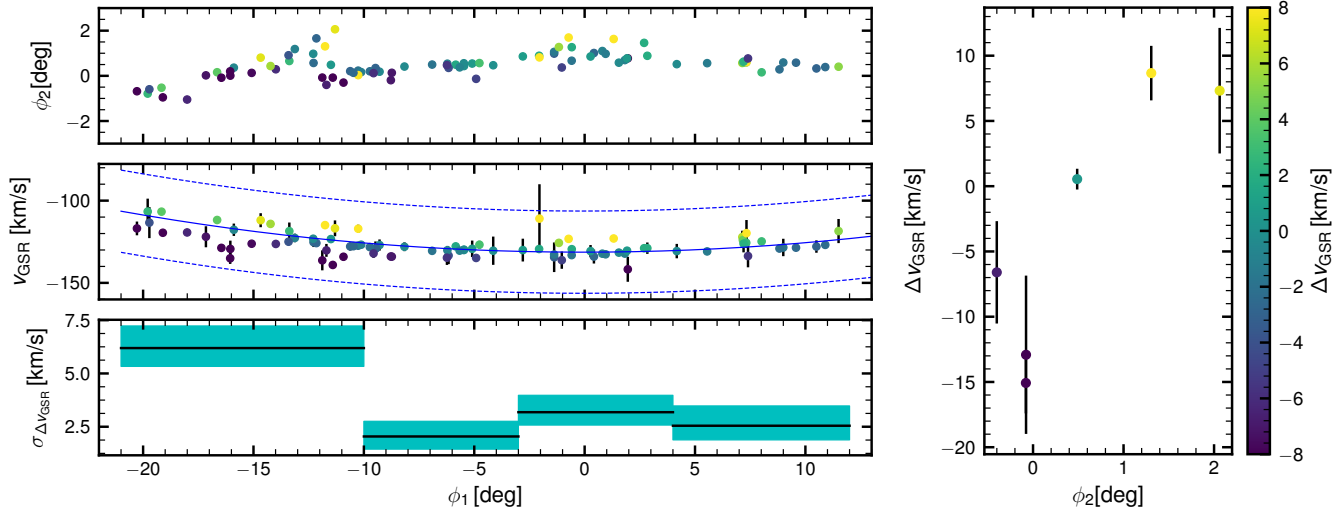


**Figure 7.** (Left) Velocity dispersion along the AAU stream. Top and middle panels show the spatial distribution and velocity distribution of the member stars, color-coded in  $\Delta v_{\text{GSR}}$ , which is derived from the difference between  $v_{\text{GSR}}$  and the best-fit RV track (blue solid line in the middle panel). Bottom panel shows the velocity dispersion of each of four portions of the stream defined based on the stream width seen in top panel, with 1- $\sigma$  uncertainties shown as the shaded regions. (Right)  $\Delta v_{\text{GSR}}$  vs.  $\phi_2$  for stars between  $\phi_1 = -12^\circ$  and  $\phi_1 = -11^\circ$ . The RVs span over  $20 \text{ km s}^{-1}$  for these six members and show a strong correlation between the position on the sky and the RVs.

count the individual metallicity uncertainties in deriving the intrinsic metallicity dispersion of the system, we again applied the same method as the one used in deriving the velocity dispersion. We found a mean metallicity of  $[\text{Fe}/\text{H}] = -2.24 \pm 0.02$  for the entire AAU stream. The metallicity dispersion is not resolved, with an upper limit of  $\sigma_{[\text{Fe}/\text{H}]} < 0.07$  at 95% confidence level. We also derive the mean metallicity and dispersion for the two components separately (with  $[\text{Fe}/\text{H}] = -2.22 \pm 0.03$  for ATLAS and  $[\text{Fe}/\text{H}] = -2.30 \pm 0.06$  for Aliqa Uma.) Aliqa Uma shows a slightly lower mean metallicity but is consistent with ATLAS within  $1.5\text{-}\sigma$  uncertainty. The posterior distribution of the mean metallicity and metallicity dispersion is shown in the right panel of Figure 8.

The low metallicity dispersion suggests that the progenitor of the AAU stream was likely a globular cluster. This conclusion is consistent with the thinness of the RGB of the stream members, low velocity dispersion found in the previous section, as well as the narrow width of the stream ( $\lesssim 100 \text{ pc}$ ).

### 2.6. Detailed Chemical Abundances

In addition to the AAT observations,  $S^5$  has also been collecting high-resolution  $R \sim 30,000$  spectroscopy on the brightest RGB stream member stars using larger aperture telescopes. Details on the observations and abundance analysis will be discussed in a forthcoming paper (Ji et al., submitted). Here we focus on a few elements that support our claim that the ATLAS and Aliqa Uma streams share a common origin. Seven stars

in ATLAS and five stars in Aliqa Uma were observed with Magellan/MIKE (Bernstein et al. 2003), producing spectra with a typical S/N of 20 per pixel in the blue and 40 per pixel in the red. In Figure 9 we show the abundance distributions for several elements. One Aliqa Uma star has especially low S/N and is thus missing from many panels. Each individual star is plotted as a thin Gaussian with its own mean and standard deviation. ATLAS and Aliqa Uma stars are shown in blue and red, respectively. The total distribution, found by summing the individual distributions, is plotted using thick blue and red lines. It is clear that both the iron abundance, and the  $[\text{X}/\text{Fe}]$  ratios for the other elements, are essentially identical between ATLAS and Aliqa Uma. Similar convergence is seen for  $\sim 10$  additional elements not shown here (Ji et al., submitted). In general the abundance scatter is smaller than expected from halo stars of similar metallicity (thick grey lines), which is most clear from the neutron-capture elements (Y, Ba, Eu).

Globular clusters exhibit characteristic element anti-correlations between stars, which we do not expect to detect in the AAU stream given our abundance uncertainties. Given the available elements and precisions, the strongest anticorrelation we expect is between  $[\text{Na}/\text{Fe}]$  and  $[\text{Mg}/\text{Fe}]$ , shown in the top-right panel of Figure 9. In some globular clusters, a 0.1 dex decrease in  $[\text{Mg}/\text{Fe}]$  corresponds to a 0.4 dex increase in  $[\text{Na}/\text{Fe}]$ , though the extent of Mg depletion varies from cluster to cluster (e.g., Bastian & Lardo 2018). Given the uncertainties

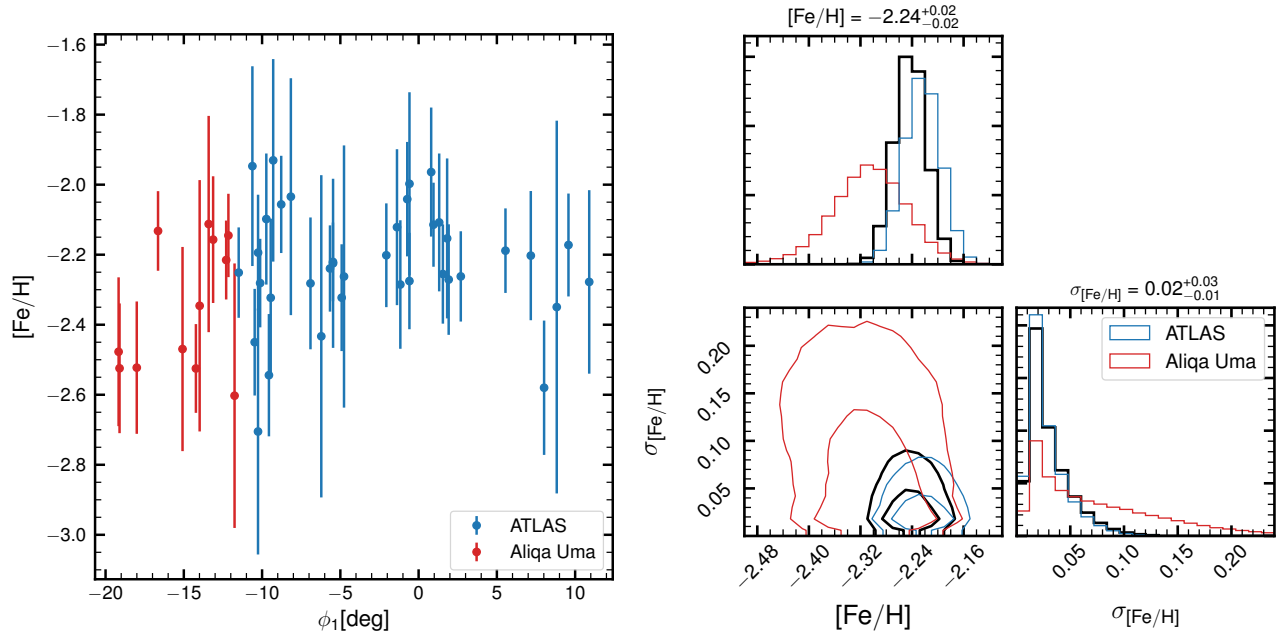


**Figure 8.** (left) Metallicity distribution as a function of  $\phi_1$  for bright RGB member stars in ATLAS and Aliqa Uma. (right) Posterior distribution of the mean metallicity and metallicity dispersion of the entire AAU stream (black), Aliqa Uma component (red) and ATLAS component (blue). The contours correspond 68% and 95% confidence interval. The numbers shown in the top and right panels are the median and 1- $\sigma$  from the posterior distribution.

in both  $[Mg/Fe]$  and  $[Na/Fe]$ , we would not expect to clearly detect this signature.

Combining the ATLAS and Aliqa Uma stars, the mean metallicity is  $-2.38 \pm 0.03$  dex with 95% confidence upper limit on the dispersion of 0.12 dex. The mean metallicity is lower than the CaT values, but within the Carrera et al. (2013) calibration systematic uncertainty of 0.16 dex.

### 3. STREAM PROPERTIES FROM GAIA DR2 AND DES DR1

In order to expand our study of the ATLAS and Aliqa Uma stream beyond the spectroscopic observations, we proceed to an analysis of the photometric and astrometric only datasets from DES DR1, PS1 DR1 and *Gaia* DR2, which allows us to probe the stream beyond the footprint coverage and depth of  $S^5$ .

#### 3.1. Isochrone Model

As a first step, we proceed to determining the DES color-magnitude diagram distribution of stream members. In Section 2.2 we have shown that the spectroscopic members line up extremely well on the RGB. In order to map the stream fully we need an isochrone model that suits both the main-sequence and RGB stars in the stream.

To find that model, we take an approximate stream track from the spectroscopic stream members

$$\text{Track}_{\phi_2}(\phi_1) = \Delta - 0.5((\phi_1 - 3)/10)^2 \text{ degrees} \quad (3)$$

where  $\phi_1$  is measured in degrees and where  $\Delta = 0.75$  for  $\phi_1 > -11.5^\circ$  and  $\Delta = 1.5$  otherwise. Then we construct the background subtracted Hess diagram for the region  $|\phi_2 - \text{Track}_{\phi_2}(\phi_1)| < 0.25^\circ$  around the track, using the two bands outside the stream region  $1^\circ < |\phi_2 - \text{Track}_{\phi_2}(\phi_1)| < 2^\circ$  as a background. We also correct the magnitudes for the distance modulus changes along the stream as measured in Section 2.3. The resulting Hess diagram is shown in Figure 10, with the absolute  $r$  magnitude and  $(g - r)$  color for spectroscopic members overplotted. The figure clearly shows a main sequence turn-off (MSTO) that smoothly transitions into the red giant branch that is well traced by the spectroscopic members.

We attempted to identify the best isochrone describing the stellar population of the stream using various isochrone sets, such as PARSEC (Bressan et al. 2012), Dartmouth (Dotter et al. 2008) and MIST (Dotter 2016; Choi et al. 2016). However, we were not able to find one that could well fit the extremely precise measurement shown on Figure 10. We therefore systematically searched for an isochrone that could match the data with the help of shifts in color and magnitude ( $g - r$ ,  $r$ ). The best match was found to be a Dartmouth isochrone

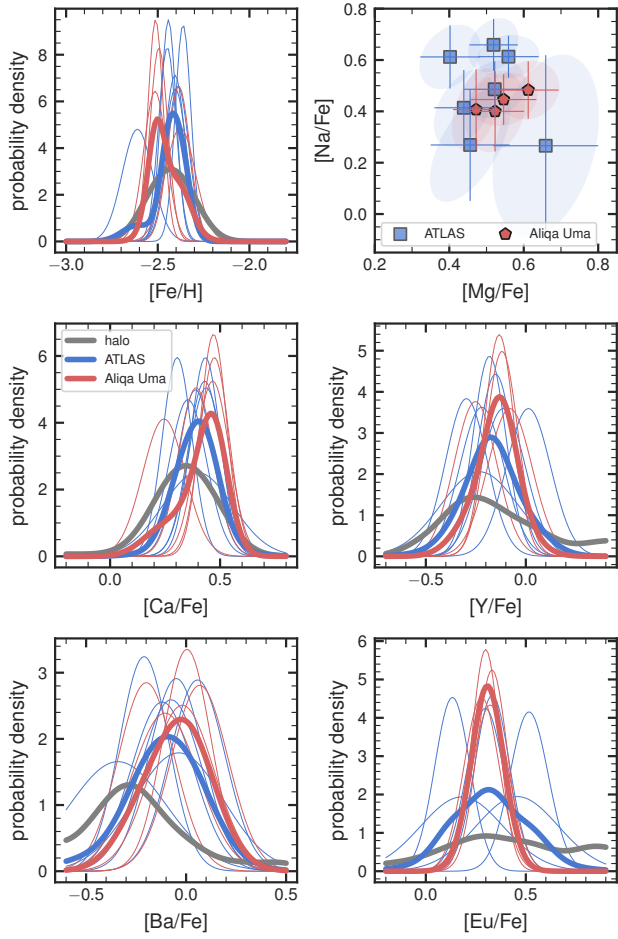


**Figure 9.** *Top right:* Elemental abundance of ATLAS stars (blue squares) and Aliqa Uma stars (red pentagons). The error bars and shaded ovals indicate  $1\text{-}\sigma$  errors propagating all stellar parameter uncertainties, including correlations in  $[\text{Na}/\text{Fe}]$  and  $[\text{Mg}/\text{Fe}]$ . *Other panels:* distribution of abundance ratios in ATLAS (blue) vs Aliqa Uma (red). Each individual star’s abundance measurement and error are treated as a Gaussian and shown as a thin colored line. The sum of these PDFs is indicated as a thick line. The thick grey line is a comparison sample of Milky Way halo stars with  $-2.55 < [\text{Fe}/\text{H}] < -2.3$  (Abohalima & Frebel 2018), a range chosen to match the MDF of ATLAS and Aliqa Uma.  $0.1$  dex errors have been assumed for the halo sample.

with parameters  $[\text{Fe}/\text{H}]=-1.99$ ,  $[\alpha/\text{Fe}]=0.4$ ,  $Y = 0.4$ ,  $\text{Age}=11.5$  Gyr<sup>5</sup> that needed to be shifted by  $0.143, 0.188$  in  $g, r$ , respectively. We remark that this shift is mostly in absolute magnitude, as the color shift is only  $\sim 0.04$ . This implies a possible mismatch in the BHB distance and MSTO distance at  $0.1$  mag level. This isochrone is shown by a red curve on the Figure. We note that the

<sup>5</sup> Filename for the best match is DECam/feh20afep4y40

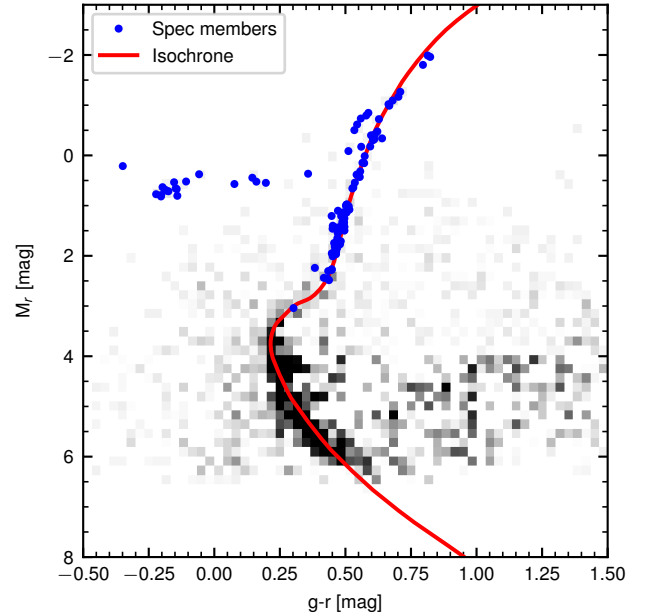


**Figure 10.** The color-absolute magnitude diagram of the ATLAS and Aliqa Uma streams from the combination of photometric and spectroscopic datasets. The greyscale image shows the background subtracted Hess diagram of the ATLAS stream for the area  $-11.5 < \phi_1 < 10$  and within  $0.25$  deg of the approximate stream track on the sky (Eq. 3). The photometric only Hess diagram is complemented by the spectroscopic members of ATLAS and Aliqa Uma shown in blue circles. The red curve is the best isochrone that matches both the main sequence stars from the deep photometric data as well as the giants from the spectroscopic sample (see main text for details). The magnitudes in this plot have been corrected by the distance modulus as a function of  $\phi_1$  determined in Section 2.3.

isochrone match is performed to get an isochrone track for the density map construction in next Section; the isochrone parameters such as metallicity,  $\alpha$ -abundance and age may not be best estimates of the properties the AAU stream, since shifts in magnitude and color are applied to get the best matching isochrone.

### 3.2. Probable stream members with Gaia

We start by constructing a map of the stellar streams using the *Gaia* astrometric data combined with accurate ground-based photometry. For this we will rely on the results from Section 2, where we determined the track of the stream in proper motion and distance space, as well as on the stream isochrone, established in the previous section.

Our primary astrometric selection based on proper motions and parallax is:

$$|\mu_\alpha - \text{Track}_{\mu,\alpha}(\phi_1)| < 0.2 + 2\sigma_{\mu,\alpha}$$

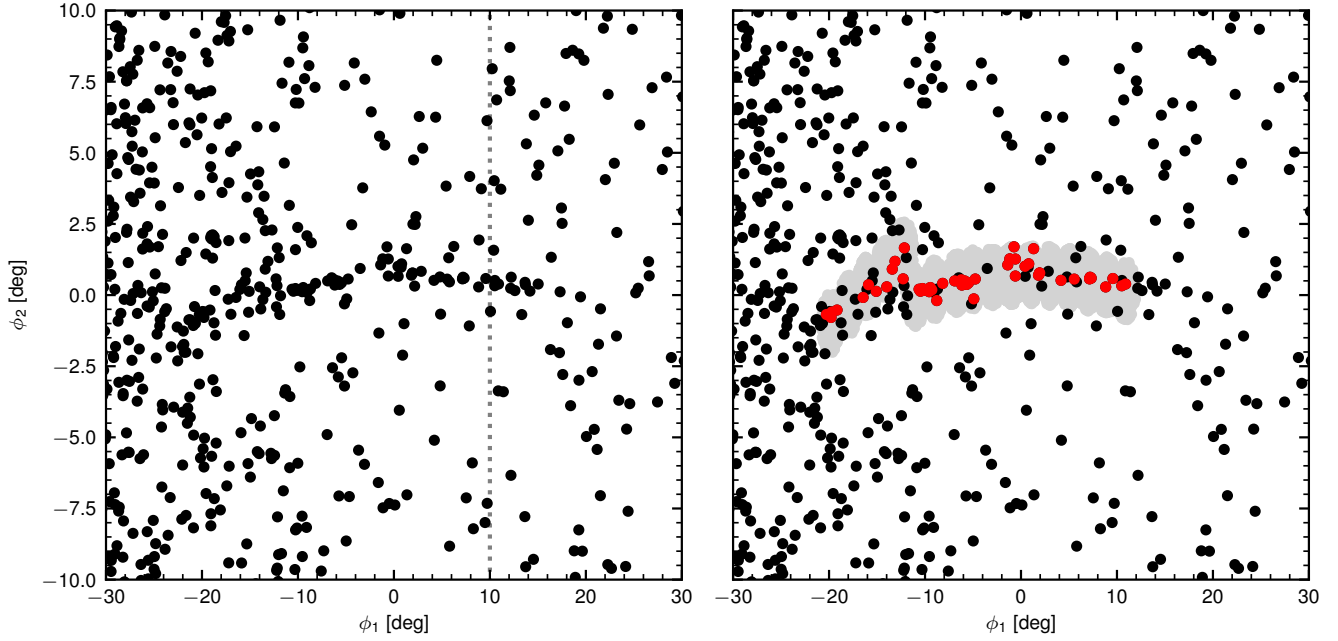


**Figure 11.** The distribution of stars on the sky in the region near the AAU stream, selected using astrometry from *Gaia* DR2 and photometry from PS1 and DES DR1 (identical for both left and right panels). As comparison, on the right panel we also show in grey the location of the  $S^5$  fields and mark in red the stars among the selected ones that are spectroscopic members identified in Section 2.2. The dashed line at  $\phi_1 = 10$  shows the boundary of the DES footprint. To the left of the line we use the photometry from DES, and to the right of the region we use the PS1 photometry. We remark that the stream is clearly extending well beyond our spectroscopic coverage to  $\phi_1 \sim 20^\circ$ , and potentially to  $\phi_1 < -20^\circ$ .

$$|\mu_\delta - \text{Track}_{\mu,\delta}(\phi_1)| < 0.2 + 2\sigma_{\mu,\delta}$$

$$\omega < 0.05 + 2.5\sigma_\omega$$

where the proper motion is in  $\text{mas yr}^{-1}$ . We then combine it with the color-magnitude selection based on photometric data from different ground-based imaging surveys. As the DES DR1 data is only available for the region of the stream with  $\phi_1 < 10^\circ$ , we were required to use photometric measurements from other surveys in the region  $\phi_1 > 10$ . We decided to rely on the PS1 photometry provided in the `MeanObject` table. The DES and PS1 color-magnitude selection is  $M_r(\phi_1) < 2$  and  $|g - r - I_{g-r}(r - \text{Track}_{dm}(\phi_1))| < 0.02$  where  $I_{g-r}(M_r)$  is the best isochrone predicted color for a given  $M_r$  as described in the previous section. Furthermore, we used simple linear corrections determined from a DES/PS1 overlap to convert the DES isochrone into the PS1 photometric system ( $g_{\text{PS1}} = g_{\text{DES}} - 0.05(g_{\text{DES}} - r_{\text{DES}})$ ,  $r_{\text{PS1}} = r_{\text{DES}} + 0.08(g_{\text{DES}} - r_{\text{DES}})$ ).

Figure 11 shows the density of likely AAU stream members according to the combined astrometric and color-magnitude selection. We also mark the stars that are identified as spectroscopic members in red (right panel). We see that the *Gaia* selected stars clearly show both the ATLAS and Aliqa Uma streams. We also see that the spectroscopic members trace the streams well,

without missing significant parts. However, there is a somewhat overdense area at  $-25^\circ < \phi_1 < -10^\circ$  below the Aliqa Uma stream, where there could be more unidentified members. Also the *Gaia* selected stars seem to show a possible “spur” — stars offset from the main stream track — at  $\phi_1 = -10^\circ$ ,  $\phi_2 \sim 2^\circ$  coming out of the continuation of the Aliqa Uma stream, and for which we could be possibly missing some members. Furthermore, the data suggests that the stream extends significantly further than indicated by the DES data, by  $> 10$  degrees up to  $\phi_1 \sim 20^\circ$ , supporting what was seen in PS1 data by Bernard et al. (2016).

### 3.3. Spatial density map with DES

Having used the *Gaia* data to map the brightest members in the AAU stream, we now proceed to use the deep DES data alone (which extends below the MSTO of the stream) to extract the stream track and density variations. To select only point sources from DES we apply the following two selections.

$$\left| \frac{S_G}{SE_G^2} + \frac{S_R}{SE_R^2} \right| \times \left( \frac{1}{SE_G^2} + \frac{1}{SE_R^2} \right)^{-1} < 0.003 \quad (4)$$

$$|r - i - 0.04 - 0.4(g - r - 0.25)| < 0.1 \quad (5)$$



where  $S_G, S_R, SE_G, SE_R$  are the SPREAD\_MODEL quantities in  $g$  and  $r$  filters and their uncertainties respectively. The first selection is a morphological selection (Desai et al. 2012; Koposov et al. 2015), while the latter is a stellar locus selection.

To proceed with the mapping we use several ingredients that we have determined in previous sections, such as the isochrone model of the stream determined in Section 3.1 and the distance track determined in Section 2.3. With this we can construct the probability distribution of stream members in CMD space as a function of  $\phi_1$ ,  $\mathcal{P}(g-r, r|\phi_1, \text{stream})$ . We can also construct the color-magnitude distribution model of the background  $\mathcal{P}(g-r, r|\text{background})$  (we assume that the background color-magnitude distribution does not depend on  $\phi_1$ ). With these two probability distributions we can use the matched filter approach from Rockosi et al. (2002) where we weight each star by the ratio of  $\mathcal{P}(g-r, r|\phi_1, \text{stream})$  and  $\mathcal{P}(g-r, r|\phi_1, \text{background})$ . We however adopted instead the binary matched filter method from Erkal et al. (2017), in which a weight of one is assigned to stars with  $\mathcal{P}(g-r, r|\phi_1, \text{stream})/\mathcal{P}(g-r, r|\text{background}) > T$  where  $T$  is the threshold chosen to maximize the signal to noise of the map, and zero otherwise. The advantage of the latter approach is that it produces a map with Poisson distributed values.

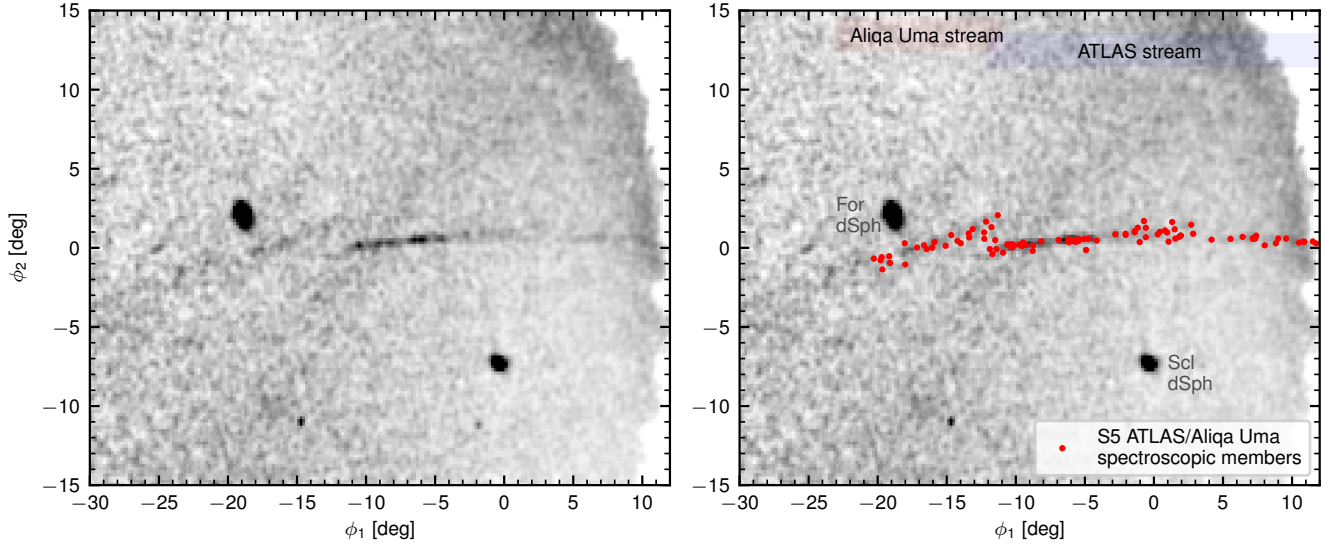
When applying the matched filter to the data we split the considered  $\phi_1$  range into 100 intervals, and for each interval of  $\phi_1$  we compute an optimal matched filter mask. The  $\phi_1$  range needs to be split because the best CMD mask will change as the stream distance changes. This should produce the optimal map of the stream, with the only caveat being that any large scale density variations along  $\phi_1$  will be somewhat modulated by the changing color-magnitude filter along  $\phi_1$ .

Figure 12 shows the matched filter map of the streams. The image has also been smoothed with a rectangular Epanechnikov kernel with a width of 3 pixels and normalized along columns to have the same mean to correct for variable stellar density along the field. Both panels show the same data, but on the right panel we also overplot the location of spectroscopic members, identified in Section 2.2. The left panel clearly shows two streams that look unconnected. However, we see that the spectroscopic members show a bridge connecting the streams. This suggests that in fact the area near  $\phi_1 \sim -12^\circ$  between two streams likely has some low-surface brightness stellar spray that is only detectable with spectroscopy. Another major feature visible on the map is density variations. We notice multiple such features. The bright part of the ATLAS stream in the range  $-12^\circ < \phi_1 < -5^\circ$  shows small-scale ( $\sim 1^\circ$ ) den-

sity oscillations, and there is an extreme density drop near  $\phi_1 \sim 3^\circ$ . We will discuss this feature later, but we remark that this density drop is accompanied by the significant broadening of spectroscopic members in  $\phi_2$ . It may also be noticed that the stream to the right of the gap at  $\phi_1 \sim 3^\circ$  is shifted down in  $\phi_2$  with respect to the stream on the left (we confirm this shift with stream track measurements at the end of this Section).

To fully characterize multiple observed features in the stream we need to construct a stream model. We follow the generative stream model approach presented in Erkal et al. (2017) and Koposov et al. (2019) based on using natural cubic splines with different numbers of knots to describe various stream properties, such as stream density, width, track and background. Specifically, we use a model implemented in the STAN programming language (Carpenter et al. 2017) that is almost identical to the one published in Koposov et al. (2019). This implementation allows us to perform the sampling of the posterior using a technique that is highly efficient in high-dimensional spaces, Hamiltonian Monte Carlo (Neal 2012; Betancourt 2017), and specifically its adaptive version called No-U-Turn Sampler (Hoffman & Gelman 2011).

Our model fits for the  $\mathcal{B}(\phi_1)$ ,  $\mathcal{B}_1(\phi_1)$ ,  $\mathcal{B}_2(\phi_1)$ ,  $\mathcal{I}(\phi_1)$ ,  $\mathcal{S}(\phi_1)$ ,  $\Phi_2(\phi_1)$  which are the splines for the logarithm of the background density, the slope of log-background across the stream, the quadratic term for the log-background, the logarithm of stream’s central stellar density, the logarithm of the stream width, and stream track on the sky, respectively. The parameters of the model are the values of the spline at the spline nodes/knots. The profile of the stream is assumed to be Gaussian along  $\phi_2$ . More details of the implementations are described in Koposov et al. (2019). The data that we model is the binned stellar density maps of matched filter selected stars (as described above). The bin-size is  $0.2^\circ$  in  $\phi_1$  and  $0.05^\circ$  in the  $\phi_2$  direction. We assume that the number counts in each pixel is a Poisson variate with the rate parameter determined by our density model. We decided to model the ATLAS and Aliqa Uma streams separately by focusing on the range of  $-21^\circ < \phi_1 < -10^\circ$  for Aliqa Uma and  $-13^\circ < \phi_1 < 10^\circ$  range for the ATLAS stream. As opposed to Erkal et al. (2017), but similarly to Koposov et al. (2019) we use equidistant spline knots. We determine the best number of knots  $k_{\Phi,2}, k_{\mathcal{I}}, k_{\mathcal{B}}, k_{\mathcal{B},1}, k_{\mathcal{B},2}$  for each spline by running Bayesian optimization (Gonzalez et al. 2016; The GPYOpt authors 2016) of the cross-validated (K=3) log-likelihood function with respect to the vector of number of knots. The cross-validation was performed by randomly assigning pixels on the sky to one of the 3 groups.



**Figure 12.** The stellar density of stars in DES DR1, selected using a  $\phi_1$ -dependent matched filter, that relies on the distance track as determined in Section 2.3 (left). The density has been computed in square bins of  $0.2^\circ \times 0.2^\circ$  and convolved with Epanechnikov kernel with the width of 3 pixels. Each column of the image was normalized by the mean background value at a given  $\phi_1$  to correct for the background density variation along  $\phi_1$ . The greyscale is linear with black corresponding to value of 4 and white to value of 0.2. The right panel shows the same stellar density map with the spectroscopic members overplotted on the stellar stream. The prominent overdensities visible on the map at  $\phi_1, \phi_2 = (0^\circ, 7^\circ)$  and  $(-19^\circ, 2^\circ)$  are Sculptor and Fornax dwarf spheroidals respectively, that are located at distances significantly further than the streams.

We only manually fix the number of knots for the stream width spline to 3 for Aliqa Uma and 15 for ATLAS. The optimization leads to  $k_{\Phi,2}, k_{\mathcal{L}}, k_{\mathcal{B}}, k_{\mathcal{B},1}, k_{\mathcal{B},2} = (10, 17, 28, 11, 3)$  nodes for the stream track, stream surface brightness, log-background, background slope and background quadratic slope for the ATLAS stream and  $(5, 5, 3, 6, 3)$  for the Aliqa Uma stream respectively. The spline models are then fitted to the data, with posterior samples computed using 12 independent chains running for 2000 iterations with the first half discarded. All the chains that we use show the satisfactory value of the Gelman-Rubin convergence diagnostic (Gelman & Rubin 1992; Gelman et al. 2013) of  $\hat{R} < 1.1$ .

The results of the model are shown in Figures 13 and 14. Figure 13 shows the best-fit model (second panel from the top) as it compares to the data (top panel) and the spectroscopic member distribution (third panel from the top). We also show that the model residuals are negligible (bottom panel). The key feature that we want to highlight is that at  $\phi_1 \sim 3^\circ$ , and possibly  $\phi_1 \sim -2^\circ$ , the model noticeably broadens, and simultaneously the spectroscopic members also show significantly broader distribution. We emphasize that the spectroscopic members are sampling much shallower data than what was used in the modeling, and therefore provide an independent assessment on these features. We also notice that our model does not detect an apparent connection between two streams, but the presence of spectroscopic

members in between the two streams at  $\phi_1 \sim -12^\circ$  suggests that there is a low surface brightness spray of stars between the streams.

To better assess the behavior of the streams captured by our model it is also informative to look at the extracted stream parameters shown in Figure 14. Here we show the stream surface brightness, on-sky track, stream width and linear density for both streams. This plot confirms several features that we have remarked on previously. The first one is we see the strong stream surface brightness variations in ATLAS. The surface brightness changes by a factor of almost 10 from one position within the main part of the stream to another. Unsurprisingly, as clearly seen in Figure 12, the surface brightness of the Aliqa Uma stream is also significantly lower than that of ATLAS. The tracks of two streams show that the Aliqa Uma stream is offset and somewhat tilted with respect to the ATLAS stream. The extracted tracks also confirm that the ATLAS stream shows a clear shift in the track at  $\phi_1 \sim 3^\circ$  of  $\sim 0.2^\circ$ , which we refer to as a “wiggle”. This shift also coincides with the observed stream broadening which is clearly visible in the stream width track in the third panel of Figure 14 as well as in Figure 13. We also notice that there is possibly another broadening at  $\phi_1 \sim -2^\circ$ , followed by narrowing near  $\phi_1 \sim 0^\circ$ . The distribution of spectroscopic members seems to support this picture, but deeper data are needed to confirm the observed behavior. There is also

a well defined overdensity in the stream at  $\phi_1 \sim 6^\circ - 7^\circ$ . This overdensity is apparent in both surface brightness and linear density and also seems to correspond to a very compact group of spectroscopic members seen in Figure 2 at  $(\phi_1, \phi_2) = (7, 0)^\circ$ . Another feature seen in Figure 14 is that the stream seems to narrow to  $\sim 0.1^\circ$  at its narrowest point at  $\phi_1 \sim -6^\circ$ . At this location the stream has the highest surface brightness and linear density. The Aliqa Uma stream seems to be significantly broader than the ATLAS stream. Finally, we also comment on the linear density profile. We notice that the linear density in ATLAS seems less variable than the surface brightness, suggesting that the main type of stream perturbation is stream broadening that does not affect the linear density significantly.

#### 4. DYNAMICAL MODELING

Equipped with measurements of the radial velocity, proper motions, distance modulus, and stream track we now fit a dynamical model to the data. In this analysis, we choose to only fit the ATLAS stream and ignore data from Aliqa Uma. This is because stream models in a smooth, time-independent Milky Way potential are not capable of reproducing the observed kink between ATLAS and Aliqa Uma. We do not attempt to separately fit Aliqa Uma since we consider this to be a perturbed part of the AAU stream. In Section 5.2 below we consider perturbations to our stream model from the Milky Way bar and giant molecular clouds which are known to perturb streams in the inner Galaxy (e.g. Amorisco et al. 2016; Erkal et al. 2017; Pearson et al. 2017).

For this fit, we use the modified Lagrange Cloud stripping code (mLCs Gibbons et al. 2014) which has been adapted to include the effect of the Large Magellanic Cloud (LMC) (Erkal et al. 2019). We take the parameters for the Milky Way model from McMillan (2017); specifically, instead of using the best-fit parameters from that work, we perform our fits on 10 posterior samples of the Milky Way potential from McMillan (2017). `galpot` (Dehnen & Binney 1998) is used to evaluate the force from this potential but we perform the stream disruption and orbit integration using the mLCs code. We model the progenitor of ATLAS as a  $2 \times 10^4 M_\odot$  Plummer sphere (Plummer 1911) with a scale radius of 10 pc, and this produces a stream with a similar width to ATLAS. For the LMC, motivated by the LMC mass measured in Erkal et al. (2019), we use a Hernquist profile (Hernquist 1990) with a mass of  $1.5 \times 10^{11} M_\odot$  and a scale radius of 17.13 kpc. This LMC model matches the observed rotation curve of the LMC at 8.7 kpc (van der Marel & Kallivayalil 2014). We compute the present-day position and velocity of the LMC using its radial velocity

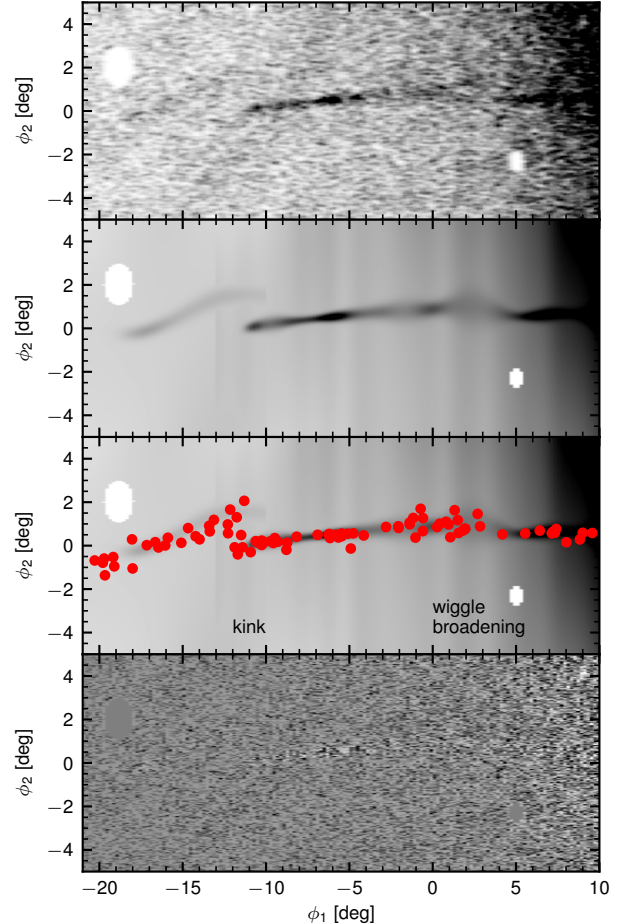


**Figure 13.** The results from modeling the density of the streams with DES DR1 photometry data. *Top panel:* The density of stream stars selected using the matched-filter mask. The panel relies on the same data as used in Figure 12, but shows only the modeled region with the same binning as used for the model fitting. *Second panel:* The maximum-a-posteriori (MAP) model of the data shown in the top panel. The model is a combination of two separate models, one for Aliqa Uma and another for the ATLAS stream. *Third panel:* The model with the spectroscopic members overplotted. *Bottom panel:* The residual density map showing the observed density minus the MAP model of the density. Two circle-shaped gaps seen in the data and models in all panels at  $(\phi_1, \phi_2) = (-19^\circ, 2^\circ)$  and  $(\phi_1, \phi_2) = (5^\circ, -2.5^\circ)$  show the masked regions around Fornax dwarf spheroidal and NGC 288 globular cluster, respectively.

(van der Marel et al. 2002), proper motions (Kallivayalil et al. 2013), and distance (Pietrzyński et al. 2013).

For the data, we use the radial velocity and proper motion of the spectroscopically confirmed members from Section 2.2. For the on-sky position, we use the stream track measured in Section 3.3, which is more precise than using the location of the spectroscopically con-

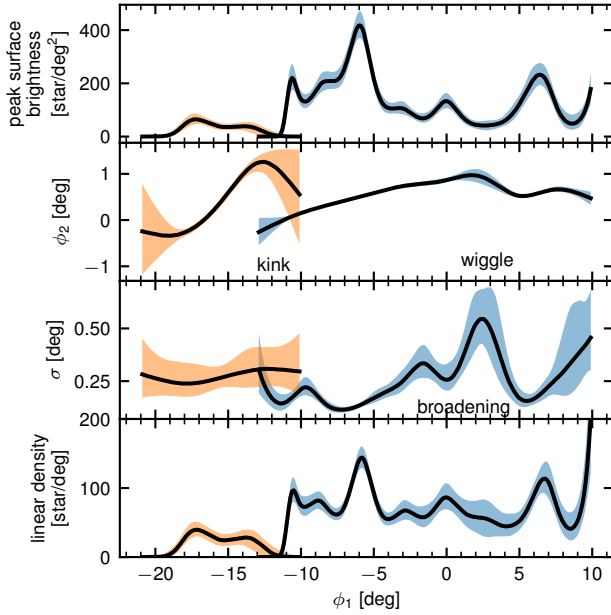


**Figure 14.** Measurement of stellar stream parameters as function of the position along the stream from modeling the density maps based on DES DR1 photometry. From top to bottom are stream surface brightness, stream track, stream width, and linear density, respectively. The shaded area shows the 1-sigma uncertainty from the posterior distribution. We remark that the stream densities shown here are for the optimal matched filter selection from DES data that is smoothly changing as a function of  $\phi_1$ , since the stream distance changes. Because of that, large scale density trends (tens of degrees) are not representative of the overall stream surface brightness changes, while small scales robustly show over- and under-densities.

firmed members. For the distance we use the polynomial for the distance measurement of Eqn. 2 with its associated covariance matrix for polynomial coefficients.

We compute the likelihood of each model stream by making mock observations and comparing this with the data. The log likelihood for each data point is

$$\log \mathcal{L}_i = -\frac{1}{2} \log \left( 2\pi(\sigma_{i, \text{obs}}^2 + \sigma_{i, \text{sim}}^2) \right) - \frac{1}{2} \frac{(m_{i, \text{obs}} - m_{i, \text{sim}})^2}{\sigma_{i, \text{obs}}^2 + \sigma_{i, \text{sim}}^2}, \quad (6)$$

where  $m_{i, \text{obs}}$  is the observed value (e.g. the radial velocity of a star),  $\sigma_{i, \text{obs}}$  is the uncertainty on the observed value,  $m_{i, \text{sim}}$  is the value of the mock observation in the simulation, and  $\sigma_{i, \text{obs}}$  is the uncertainty on the mock observation.

For the track on the sky, the data we use is the spline fit to the stream track from Section 3.3. We fit a line using least squares to the simulated stream particles within

$1.28^\circ$  in  $\phi_1$  of each node of the stream track to determine the sky position of the simulated stream and its associated uncertainty on the mean. The observed value at the node and its uncertainty are then compared with simulated value and its uncertainty using Eqn. 6.

For the proper motions and radial velocities, we use the measurements for each star. We fit a line to mock observations of the simulated stream within  $1.26^\circ$  of each star. This linear fit gives the mean and standard deviation of the mock observable at the location of the star. To compute the likelihood we then compare the observed radial velocity (proper motion) and its associated uncertainty with the velocity (proper motion) of the simulated stream at that location. We use the width of the mock observable as  $\sigma_{i, \text{sim}}$ . Finally, for the distance modulus we make a mock observation of the distance and fit a quadratic over the same  $\phi_1$  range as the BHBs and RRLs in ATLAS (see Figure 6). We then compare this with the observed fit, accounting for the covariance in both the model and the data.

We explore the likelihood space using the MCMC code `emcee` (Foreman-Mackey et al. 2013). We stress that for each MCMC we performed, we used a fixed Milky Way potential so we are not fitting the potential but instead finding the best stream in that potential. We choose to place the progenitor of the stream at  $\phi_{1, \text{prog}} = 0^\circ$  and thus our free parameters are the progenitor’s other coordinate on the sky ( $\phi_{2, \text{prog}}$ ), radial velocity ( $v_{r, \text{prog}}$ ), proper motions ( $\mu_{\alpha, \text{prog}}^*, \mu_{\delta, \text{prog}}$ ), and distance ( $d_{\text{prog}}$ ). We take a normally distributed prior on the distance of  $(22.9 \pm 1 \text{ kpc})$  from the measurement in Shipp et al. (2018). For the proper motions and radial velocity we use uniform priors which are broad,  $|\mu_{\alpha}^*| < 10 \text{ mas yr}^{-1}, |\mu_{\delta}| < 10 \text{ mas yr}^{-1}$ , and  $|v_r| < 500 \text{ km s}^{-1}$ . We give a uniform prior on  $\phi_{2, \text{prog}}$  with  $-2^\circ < \phi_{2, \text{prog}} < 2^\circ$ . We use 100 walkers for 2000 steps with a burn-in of 1000 steps. We note that for all of the subsequent analysis in this work, we only use the Milky Way realization from McMillan (2017) which gave the best-fit to AAU.

Figure 15 shows the best-fit stream model compared to the data. In each panel we show mock observations of the simulated stream against the observations. For the radial velocity component, the difference between the observed data and the model is shown for better presentation. The model fits the data along the entire ATLAS portion of the stream well. It also matches the observed properties of Aliqa Uma apart from the track on the sky, showing that these two streams are one and the same.

This model highlights the peculiar features observed in the ATLAS stream discussed in Sections 2 and 3. First,



the model does not capture the increased width or the wiggle in the stream track at  $\phi_1 \sim 3^\circ$ . Furthermore, near the connection between ATLAS and Aliqa Uma ( $\phi_1 \sim -12^\circ$ ) the observed radial velocity is more negative than the simulated velocity, supporting the interpretation in Figure 7 that the radial velocity shows signs of a perturbation. Finally, this model passes through the possible continuation of AAU to  $\phi_1 \sim 20^\circ$  shown in Figure 11.

We can also use the results of the MCMC to measure the orbital properties of the AAU stream. We find a pericenter of  $13.3^{+0.1}_{-0.2}$  kpc, an apocenter of  $41.0^{+0.4}_{-0.5}$  kpc, an eccentricity of  $0.511 \pm 0.001$ , and an orbital period of  $0.62 \pm 0.01$  Gyr. The stream is on a prograde orbit with respect to the Milky Way disk. The present-day angular momentum of the progenitor has an orientation of  $(\phi, \psi) = (-11.2^{+0.4}_{-0.3}, -24.3^{+0.2}_{-0.3})^\circ$  where  $\phi, \psi$  are the longitude and latitude as viewed from the Galactic center. As a consistency check, we also fit a plane to the best-fit stream particles in the observed range ( $-20^\circ < \phi_1 < 10^\circ$ ) through the Galactic center and found a normal orientation of  $(-5.2^\circ, -24.9^\circ)$ . This slight misalignment of the stream plane and its angular momentum is due to the effect of the LMC. We note that the orientation of AAU is broadly similar to the plane found in Shipp et al. (2018) for ATLAS, who found  $(-22.7^\circ, -21.5^\circ)$  using photometric data from DES and to Pawlowski & Kroupa (2014) who found  $(-21.9^\circ, -24.8^\circ)$  using the endpoints of the stream. Given this similar orientation, it is likely that ATLAS is still consistent with being a member of the vast plane of satellites (Pawlowski & Kroupa 2014; Riley & Strigari 2020).

## 5. DISCUSSION

### 5.1. Alignment of the AAU Stream

Using the 6D view of the AAU stream from this paper, we can look at the alignment of the stream and whether the velocity is aligned with the shape of the stream. In particular, we follow the approach of Erkal et al. (2019) and de Boer et al. (2019) who showed that the alignment can be compared on the sky and along the line of sight. For the on-sky alignment, we compare the slope of the stream on the sky ( $\frac{d\phi_2}{d\phi_1}$ ) with the ratio of reflex corrected proper motions ( $\frac{\mu_2}{\mu_1}$ ). We stress that  $\mu_1$  does not contain the typical  $\cos(\phi_2)$  term. We make this comparison in the top panel of Figure 16 which shows that the on-sky velocity (solid blue lines) is misaligned with the stream track (red points). For the ATLAS portion of the stream ( $\phi_1 > \sim -13^\circ$ ), this misalignment matches the misalignment in the simulation on average.

In order to compare the alignment along the line of sight, in the bottom panel of Figure 16 we show the

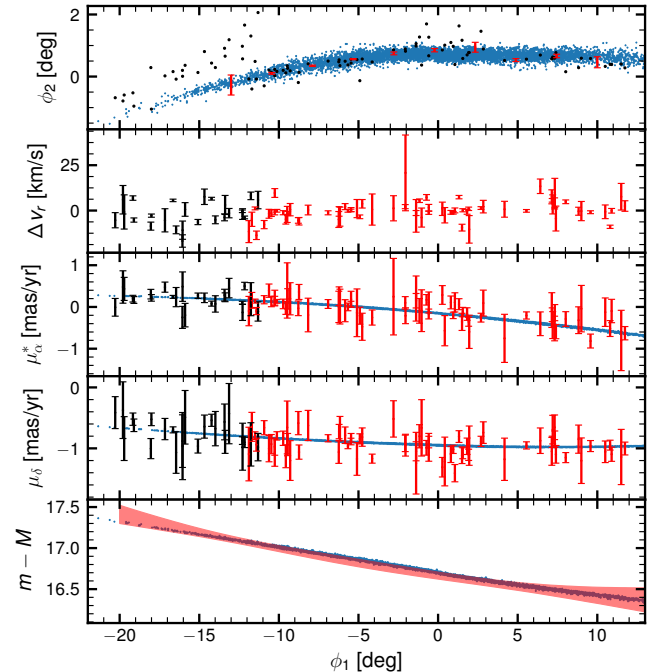


**Figure 15.** Best-fit stream model to the ATLAS stream. In each panel, the blue points show the best-fit stream model, the red-points show the data that were used in the fit, and the black points show data that was not used in the fit. *Top panel* shows the stream on the sky. *Second panel* shows the radial velocity difference between the observations and the model for clearer presentation, because the radial velocity spans a wide range. *Third panel* and *fourth panel* shows the proper motion in right ascension and declination respectively. *Bottom panel* shows the distance modulus to the stream. The red shaded region shows the  $1\text{-}\sigma$  uncertainty on the distance modulus. Note that the continuation of the ATLAS stream model is a good match to most of the observed properties of the Aliqa Uma stream apart from the track on the sky (top panel).

distance gradient of the stream ( $\frac{dr}{d\phi_1}$ ) (in blue) with the ratio of the Solar reflex corrected velocity and proper motion ( $\frac{v_r}{\mu_1}$ ) (in red). This shows that the velocity is aligned with the stream along the line of sight, as is expected from the simulation. However, since the uncertainties are large, improving the distance gradient will make this comparison more meaningful. We note that the misalignment in the simulation at  $\phi_1 \sim 0^\circ$  is due to the progenitor.

### 5.2. Perturbation by baryonic substructures

In order to check whether the perturbations in AAU could be due to baryonic substructure in the Milky Way, we consider a variety of perturbers which can affect streams. In particular, we consider the effect of the bar (e.g. Hattori et al. 2016; Price-Whelan et al. 2016; Erkal



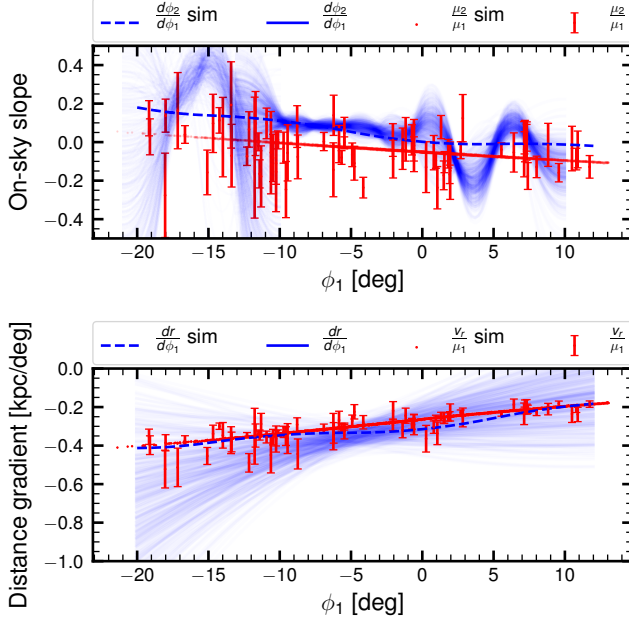


**Figure 16.** Alignment of the AAU stream’s velocity and shape. *Top panel* compares the stream velocity and shape on the sky which shows that the stream is increasingly misaligned for smaller  $\phi_1$ . The solid and dashed blue lines show the slope of the stream on the sky ( $\frac{d\phi_2}{d\phi_1}$ ) in the data and best-fit simulation respectively. For the data we show 500 realizations of the slope drawn from the spline fit in Section 3.3. The red error bars and red points show the ratio of the reflex corrected proper motions ( $\frac{\mu_2}{\mu_1}$ ) in the data and best-fit simulation respectively. *Bottom panel* compares the stream velocity and shape along the line of sight which shows that the stream is broadly aligned in this direction. However, we note that there is a large uncertainty in the distance gradient. The solid and dashed blue lines show the distance gradient of the stream on the sky ( $\frac{dr}{d\phi_1}$ ) in the data and best-fit simulation. For data, we show 500 realizations of the distance gradient drawn from the polynomial fit in Eq. 2 and its associated covariance. The red error bars and red points show the ratio of the reflex corrected radial velocity to the proper motion along the stream ( $\frac{v_r}{\mu_1}$ ) in the data and best-fit simulation. For the best-fit simulation, there is a slight misalignment near  $\phi_1 \sim 0^\circ$  due to the location of the progenitor. Note that in both panels we have only included stars with  $g < 19$ .

et al. 2017; Pearson et al. 2017), spiral arms (Banik & Bovy 2019), giant molecular clouds (GMCs, Amorisco et al. 2016), classical satellites, and globular clusters. Interestingly, while a number of these mechanisms can create subtle features in the stream, we find that of the mechanisms considered, only the Sagittarius dwarf is capable of creating the kink feature.

### 5.2.1. Milky Way bar

For the bar we consider the analytic bar potential from Long & Murali (1992). Following Hattori et al. (2016); Erkal et al. (2017) we use a semi-major axis of  $a = 3$  kpc and a semi-minor axis of  $b = 1$  kpc for the bar. For the mass, we use the recent results of Portail et al. (2017) and take a bar mass of  $10^{10} M_\odot$ . For the pattern speed, we use  $\Omega = 41 \pm 3 \text{ km s}^{-1} \text{ kpc}^{-1}$  from Sanders et al. (2019) which is consistent with other recent measurements (e.g. Portail et al. 2017; Bovy et al. 2019). We take the bar’s present-day orientation to be  $30^\circ$  (Wegg et al. 2015). When including the bar, we set the bulge mass to zero.

In order to account for the uncertainty in AAU’s orbit, we sample the MCMC chains from Section 4 100 times. For each of these samples, we also sample the bar’s pattern speed from its observed value and uncertainty. Since the bar slightly changes the mass distribution of the Milky Way potential, we compare these streams with those disrupted in the presence of a rapidly rotating bar ( $\Omega = 1000 \text{ km s}^{-1} \text{ kpc}^{-1}$ ).

For each of the 100 realizations, we compute the change in the stream track measured at the  $\phi_1$  locations of the nodes from the fit in Figure 14. The maximum change amongst all realizations is  $0.1^\circ$  and the median of the maximum change for each realization is  $0.03^\circ$ . This shows that the bar is not capable of creating the kink between ATLAS and Aliqa Uma. Similarly, we compare the stream density in 1 degree bins and find that the median of the maximum change in the density is  $\sim 25\%$ . Thus, while the bar should not have a significant effect on the stream track of AAU, it can create modest density variations.

### 5.2.2. Giant Molecular Clouds (GMCs)

For the GMCs we take a similar approach to Banik & Bovy (2019). In particular, we take the catalog of observed GMCs from Miville-Deschênes et al. (2017). Since AAU has a pericenter of  $\sim 13$  kpc, we only consider the GMCs with galactocentric radii beyond 10 kpc. We only consider GMCs with mass greater than  $10^5 M_\odot$  since perturbers below this mass will not create significant features in the stream (Erkal et al. 2016; Bovy et al. 2017). As in Banik & Bovy (2019) we consider the GMC population within the same quadrant as the Sun which is the most complete. However, instead of replicating this quadrant, for each GMC in this patch we create 4 copies by randomly sampling its azimuthal angle. This gives 624 GMCs beyond 10 kpc with a mass larger than  $10^5 M_\odot$ . We model each GMC as a Plummer sphere with the observed mass and a scale radius which is one-third that of the observed size. This reduced size means that 90% of each GMC’s mass is within the ob-

served size (Banik & Bovy 2019). Each GMC is then placed on a circular orbit in the plane of the disk. The influence of all GMCs is included during the rewinding procedure and subsequent stream generation.

As with the bar in Section 5.2.1, we consider the same 100 realizations of the AAU stream in order to account for the variation in the stream orbit. The addition of these GMCs slightly changes the mass distribution of the Milky Way potential so we once again consider a rapidly rotating population of GMCs as our fiducial setup to account for the smooth change in the potential. To do this, we keep the GMCs on their original circular orbits but increase the angular velocity by a factor of 100. As with the bar, we compare the change in the stream track and the stream density. For the stream track, we get a maximum difference of  $0.04^\circ$  and a median of the maximum change for each realization of  $0.008^\circ$ . Thus the present day distribution of GMCs do not appear to be capable of creating the kink. This is due to a combination of the modest mass of the GMCs as well as the assumption that the GMCs are confined to the Milky Way plane while AAU is on a highly inclined orbit. As a result, there will always be a significant relative velocity between AAU and the GMCs at closest approach which will limit the size of the perturbation (e.g. Erkal & Belokurov 2015b). The median of the maximum density change is  $\sim 20\%$ , indicating that GMCs can also make modest density features in the stream.

### 5.2.3. *Spiral arms*

In order to assess the impact of spiral arms, we follow largely the same procedure as Banik & Bovy (2019). Namely, we use the analytical spiral arm potential from Cox & Gómez (2002) and implement it following a sinusoidal density distribution. As in Monari et al. (2016), we use tightly wound spirals with a constant pitch angle of  $9.9^\circ$  and fix their amplitude such that the maximum force from the spirals at a distance of 8 kpc from the Galactic center is 1% of the disk force at that distance. This amplitude is determined using spirals arms with scale lengths and heights of 3 kpc and 0.3 kpc respectively, as used by Banik & Bovy (2019). We randomly sample the pattern speed 100 times from a Gaussian with  $\Omega_{\text{spiral}} = 22 \pm 2.5 \text{ km s}^{-1} \text{ kpc}^{-1}$ . As with the Milky Way bar in Section 5.2.1, we consider a fiducial setup with a pattern speed of  $\Omega_{\text{spiral}} = 1000 \text{ km s}^{-1} \text{ kpc}^{-1}$  to account for any smooth change to the potential due to the spirals. For the stream track, we find a maximum change of  $0.02^\circ$  and for the density there is a median maximum change of 7%. This shows that spiral arms cannot significantly affect the AAU stream.

### 5.2.4. *Classical satellites*

In order to assess the impact of the 10 classical satellites (excluding the LMC), we include each satellite as an additional perturber. Motivated by the results of Law & Majewski (2010), each satellite is modeled as a  $10^9 M_\odot$  Plummer sphere with a scale radius of 1 kpc. This is not meant to perfectly represent each satellite, but rather to check whether they can create a feature qualitatively like the kink. We note this neglects the effect of the tidal debris from the dwarf on AAU (Bovy 2016) which may be important in the event of a close flyby. For the proper motions, we use the results of Gaia Collaboration et al. (2018c) except for Leo I, Leo II, and the SMC for which we use proper motions from Sohn et al. (2013); Piatek et al. (2016); Kallivayalil et al. (2013), respectively. The other properties come from McConnachie (2012) and references therein. For simplicity, we do not consider ultra-faint dwarfs.

We use the same 100 realizations of AAU's orbit from Section 5.2.1. For each realization, we sample the observed properties of each dwarf (i.e. distance, radial velocity, and proper motions). The effect of the dwarf on the progenitor, Milky Way, and LMC is included during the rewinding procedure and on the stream during the disruption. Note that we consider the effect of each of the 10 dwarfs separately so this results in 1000 stream disruptions. For each stream, we compute the change in the stream track and the stream density. We find that only Sagittarius can have a large effect on the stream track with a maximum track deviation of  $\sim 1^\circ$  while the other dwarfs have a maximum deviation of  $0.06^\circ$ . Interestingly, 6 of these realizations of Sagittarius produce kink-like features in AAU, although not at the observed location of  $\phi_1 \sim -12^\circ$ .

In order to study the effect of Sagittarius more closely, we take the phase-space coordinates (i.e. proper motions, distance, and radial velocity) of one of the original realizations which produces a kink and resample about these values 1000 times with 10% of the observed uncertainties. We then make mock observations of these in each observable (e.g. as in Figure 15) and select those with a kink at  $\phi_1 \sim -12^\circ$  based on visual inspection.

Figure 17 shows the mock observations for one of these realizations that qualitatively matches the observed properties of AAU with a kink in the stream track, a  $\sim 10 \text{ km/s}$  change in the radial velocity, and a kink in the distance modulus all at  $\phi_1 \sim -12^\circ$ .<sup>6</sup> We note that the model does not match the radial velocity to the left of  $\phi_1 \sim -12^\circ$ . This kink is the result of

<sup>6</sup> A movie of this simulation is available at <https://youtu.be/GjZJYEQQZXU>

a close approach between Sagittarius and AAU  $\sim 0.51$  Gyr ago at a distance of  $\sim 0.9$  kpc with a relative velocity of  $\sim 400$  km/s. The closest approach changes the orbital period of particles in the stream and creates a gap with particles piling up at the edge of the gap (e.g. Erkal & Belokurov 2015b). One of these pile-ups occurs at  $\phi_1 \sim -13^\circ$  and creates the kink and overdensity. The other pile-up is located at  $\phi_1 \sim 25^\circ$  which is beyond the currently observed range of AAU.

We note that given the current uncertainties on the present-day phase-space position of Sagittarius, we cannot definitively determine whether or not it has interacted with AAU in the past. In order to explore this, we computed where the past orbit of Sagittarius (using the realizations above) passed through the stream plane of AAU given the uncertainty in the proper motion, radial velocity, and distance of Sagittarius. These crossings occur  $0.4 \pm 0.1$  Gyr ago with an uncertainty of 3.0 kpc in where they cross the AAU stream plane. This is mostly driven by the distance uncertainty; improving the distance errors by a factor of 2 lowers this uncertainty to 1.5 kpc. Interestingly, this uncertainty in crossing the AAU stream plane does not seem to be heavily affected by the uncertainty in the Milky Way potential. We explored this by also sampling from the posterior samples from McMillan (2017) and found the same uncertainty of 3.0 kpc. Thus, improved measurements of the phase-space location of Sagittarius will help us determine whether it created the kink in AAU.

Finally, we note that de Boer et al. (2019) have also shown that the Sagittarius dwarf could have perturbed the GD-1 stream (Grillmair & Dionatos 2006). If it can be shown that Sagittarius perturbed both GD-1 and AAU, this would place very tight constraints on the orbit of Sagittarius as well as the potential of the Milky Way.

### 5.2.5. Globular clusters

Similar to the classical dwarf galaxies in Section 5.2.4, we also consider the population of globular clusters in the Milky Way as potential stream perturbers. For this we use the globular cluster catalog of Vasiliev (2019a) which gives the 6D phase-space positions of 147 globular clusters. For each of the 100 realizations of AAU's orbit from Section 5.2.1, we sample the observed properties of each globular cluster and include the cluster during the rewinding and stream disruption process. As with the dwarfs in Section 5.2.4, we include the globular clusters one at a time so this results in 14700 stream disruptions. To be conservative, we model each cluster as a Plummer sphere with a mass of  $10^6 M_\odot$  and a scale radius of 10 pc.

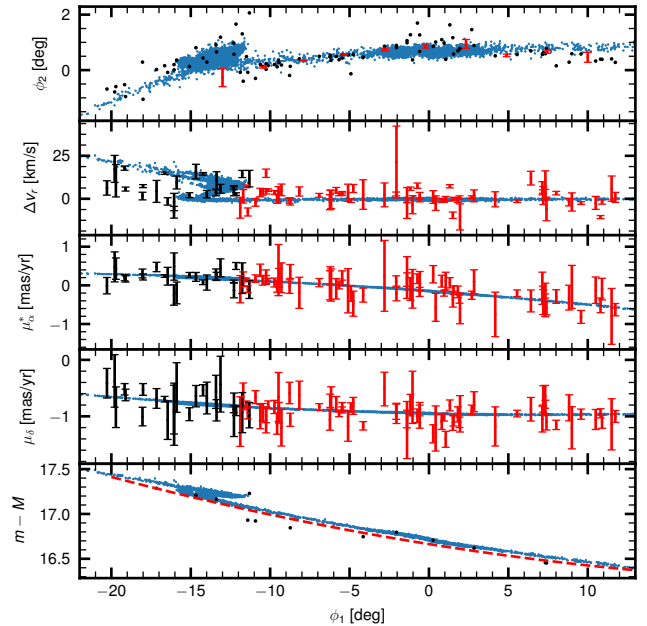


**Figure 17.** Example of perturbation from the Sagittarius dwarf on the ATLAS stream. This realization was chosen to have a kink at  $\phi_1 \sim -12^\circ$  (see text for details). The panels show the same mock observables as in Figure 15 apart from the radial velocity where we show the difference from a quadratic function fit to the simulated stream between  $-10^\circ < \phi_1 < 13^\circ$ . In addition, we show the distance modulus of individual BHBs from Figure 6 in the bottom panel. Interestingly, this perturbation also produces a kink in the radial velocity and distance modulus similar to the observations although we note that the radial velocity in the model to the left of  $\phi_1 < -15^\circ$  does not match the observed trend.

For each simulation, we measure the simulated stream track and density, as well as how close the cluster comes to each stream particle. Four globular clusters have a median closest approach within 2 kpc: Pal 12 (1.9 kpc), NGC 5904 (1.5 kpc), NGC 6229 (1.4 kpc), and NGC 7492 (0.6 kpc).

Furthermore, we find that 16 globular clusters have closest approaches (amongst their 100 realizations) within 100 pc of the stream. For most of these globular clusters, only 1 out of 100 of the realizations pass within 100 pc, indicating that this is due to significant uncertainty in the past trajectory. However, NGC 7492 and NGC 6229 stand out, having a 17% and 7% chance of passing within 100 pc of the stream respectively.

In terms of the stream track, 8 globular clusters produce deviations which are larger than  $0.1^\circ$  with a maximum deviation of  $0.24^\circ$ . Of these, one (NGC 7492) produces a feature like a kink in the stream track with a deviation of  $0.19^\circ$ . We show this in the top panel of Figure 21 in Appendix C, while the other panels show other

perturbations from NGC 7492. Interestingly, some of these realizations also exhibit a broadening of the stream track similar to the one observed at  $\phi_1 \sim 3^\circ$  (see Figure 13). We note, however, that in the January 2020 version of the Baumgardt et al. (2019) catalogue of fundamental parameters of Galactic globular clusters<sup>7</sup>, the mass of NGC 7492 is listed as  $2.8 \pm 0.8 \times 10^4 M_\odot$  which is significantly smaller than the mass we have assumed. Thus, while globular clusters may be able to create a subtle feature in AAU, like the broadening, they cannot create the large kink at  $\phi_1 \sim -12^\circ$ .

### 5.2.6. Progenitor

Using the best-fit stream from Section 4, we can assess whether any of the features in the data are consistent with the progenitor. At the location of the progenitor, the stream will connect on at the inner and outer Lagrange points (e.g. Combes et al. 1999), which can cause a visible kink in the stream (e.g. Pal 5, Odenkirchen et al. 2001) depending on the orientation of the stream relative to the observer. For AAU, the angle between the line of sight and the radial direction from the Galactic center is  $49.0^\circ$  at  $\phi_1 = 0^\circ$  suggesting that if a progenitor was present, we would be able to see the stream connecting onto the progenitor which would appear as a wiggle near the progenitor. In order to explore this, we re-simulate the best-fit AAU model from Section 4 with progenitor masses of 2, 20,  $200 \times 10^4 M_\odot$  and force the progenitor mass to remain constant throughout the simulation. These give significant wiggles in the stream track with sizes of  $0.26^\circ$ ,  $0.56^\circ$ , and  $1.2^\circ$  respectively. In order to match the  $\sim 2^\circ$  size of the kink between ATLAS and Aliqa Uma, we would need a present-day progenitor mass of  $\sim 8 \times 10^6 M_\odot$ , over  $3\times$  more massive than the most massive known globular cluster and thus certainly ruled out (Harris 2010).

### 5.3. Connection to other globular clusters

In order to assess the relation between the AAU stream and globular clusters in the Milky Way, we compute the actions of our best-fit stream and each globular cluster. For each globular cluster, we sample the observed proper motions, distances, and radial velocities 100 times given their uncertainties to get the spread in actions. For the observed properties we use the globular cluster catalog from Vasiliev (2019a), which contains 147 globular clusters. Note that we have replaced the distance to Palomar 5 with an updated distance of  $20.6 \pm 0.2$  kpc from Price-Whelan et al. (2019). We compute the actions using AGAMA (Vasiliev 2019b).

In Figure 18 we show these actions along with that of the AAU stream. We compute the distance between AAU and each globular cluster in action space using the combined action modulus,

$$\Delta J = \sqrt{\Delta J_\phi^2 + \Delta J_R^2 + \Delta J_z^2} \quad (7)$$

We have highlighted the three globular clusters closest in action space: Whiting 1, NGC 5824, and Pal 12. Interestingly, these have previously been associated with the Sagittarius dwarf (e.g. Irwin 1999; Bellazzini et al. 2003; Carraro et al. 2007; Massari et al. 2019). Furthermore, the eccentricity and apocenter of AAU stream is very similar to the Sagittarius GCs discussed in Kruijssen et al. (2020), suggesting that the progenitor of the AAU stream may have been originally bound to the Sagittarius dwarf. In further support of this, we note that the mean metallicity of AAU is similar to that of one of the GCs associated with Sagittarius, Terzan 8 (e.g. Massari et al. 2019), which has a metallicity of  $[\text{Fe}/\text{H}] \sim -2.27$  (Carretta et al. 2014).

### 5.4. Complex stream morphologies

Recent works have shown that almost every stream studied in detail has signs of a significant perturbation. Pal 5 shows clear gaps which are inconsistent with evolution in a smooth, time-independent potential (e.g. Erkal et al. 2017; Bonaca et al. 2020). GD-1 has a spur of stars that run parallel to the stream and a blob of co-moving stars below the stream, as well as wiggles and density variations (e.g. de Boer et al. 2018; Price-Whelan & Bonaca 2018; Malhan et al. 2019; de Boer et al. 2019). The Ophiuchus stream also exhibits a spur-like feature parallel to the main track (Caldwell et al. 2020). This appears to support the models of Carlberg (2020), which predict that globular cluster streams have a rich morphology due to their initial disruption in their host dwarf galaxy before being accreted into the Milky Way.

Similarly, streams from dwarf galaxies also show rich structures. The Sagittarius stream exhibits a prominent bifurcation (Belokurov et al. 2006) and the Jhelum stream appears to have multiple components (Bonaca et al. 2019a; Shipp et al. 2019). In addition, the Orphan stream has a substantial velocity perpendicular to the stream (Fardal et al. 2019; Koposov et al. 2019) due to the perturbation from the LMC (Erkal et al. 2019). Similarly, many of the streams discovered in DES exhibit substantial misalignment between the stream track and the on-sky velocity, likely due to the LMC (Shipp et al. 2019), including the AAU stream, as we discussed in Section 5.1.

### 5.5. Palca stream in the Aliqa Uma stream field

<sup>7</sup> <https://people.smp.uq.edu.au/HolgerBaumgardt/globular/>



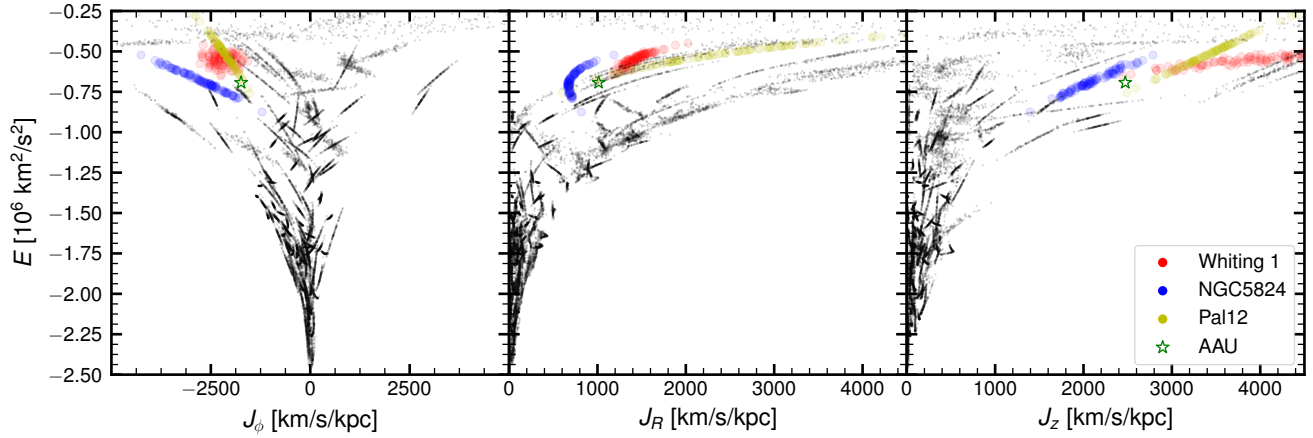


**Figure 18.** Actions for 147 Milky Way globular clusters and the best-fit to the ATLAS stream. For each globular cluster, we have sampled their actions 100 times given the uncertainties on their present day proper motions, distances, and radial velocities using the catalog from [Vasiliev \(2019a\)](#). The green star shows the actions for our best-fit orbit for AAU stream. The red, blue, and yellow points show the actions of the globular clusters closest to AAU in action space, Whiting 1, NGC 5824, and Pal 12, respectively. Interestingly, these are all associated with the Sagittarius dwarf (e.g. [Irwin 1999](#); [Bellazzini et al. 2003](#); [Carraro et al. 2007](#); [Massari et al. 2019](#)), suggesting that the progenitor of AAU stream may have been accreted with the Sagittarius dwarf. The black points show the actions of the remaining 144 globular clusters.

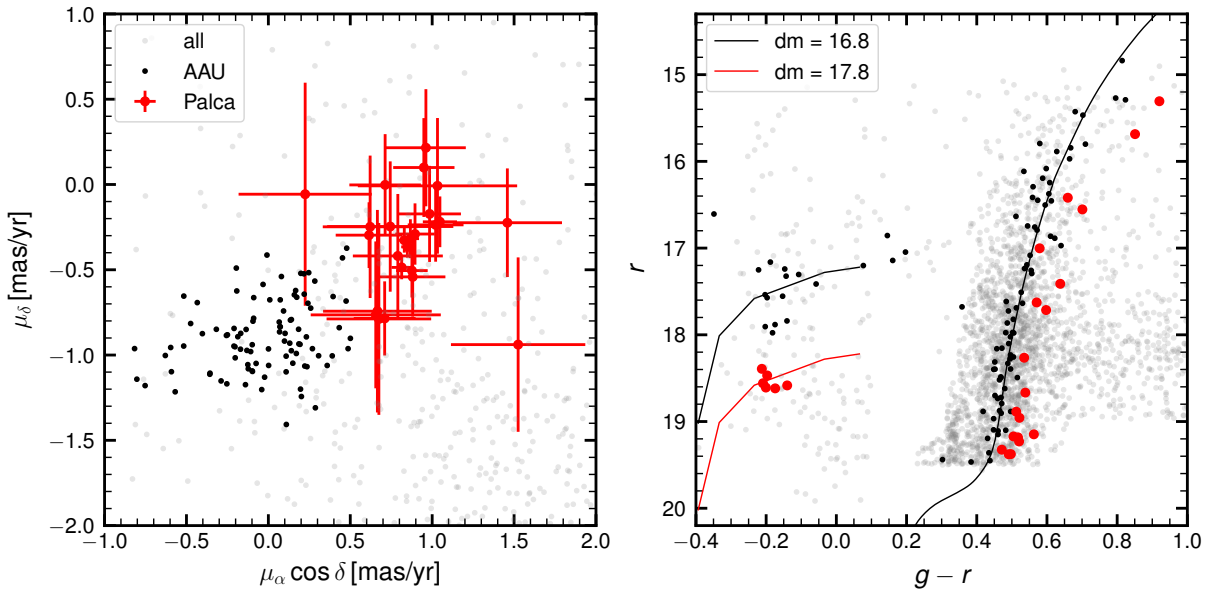


**Figure 19.** Proper motions (left) and CMD (right) of the other structure discussed in Figure 1. Stars with  $80 < v_{\text{hel}} < 130 \text{ km s}^{-1}$  are selected and shown as the red circles with error bars. These stars are also clustered in proper motion space with a distance modulus of 17.8, and are likely to be member stars of the Palca Stream. The grey dots show all observed stars, while black dots represent the spectroscopic members in the AAU stream.



As discussed at the beginning of this paper, in Figure 1, when selecting high priority candidate members in AAU, we also see substructure in velocity around  $v_{\text{hel}} \sim 100 \text{ km s}^{-1}$ , especially in the fields of the Aliqa Uma stream. These stars are also clustered in proper motion space around

$$\mu_{\alpha} \cos \delta = 0.85 \text{ mas yr}^{-1}$$

$$\mu_{\delta} = -0.37 \text{ mas yr}^{-1}$$

The proper motion is very close to the AAU stream and therefore some were selected as high priority candidates. Figure 19 shows the stars with the following selection criteria

$$80 < v_{\text{hel}} < 130 \text{ km s}^{-1}$$

$$|\mu_{\alpha} \cos \delta - 0.85| < \max(0.3, 2\sigma_{\mu, \alpha})$$

$$|\mu_{\delta} + 0.37| < \max(0.3, 2\sigma_{\mu, \delta})$$

and

$$-20^{\circ} < \phi_1 < -10^{\circ}$$

We found a very clear stellar association at a distance modulus of  $m - M \sim 17.8$  in the CMD (right panel of the Figure), further confirming that this is a real structure rather than just a random clustering in line-of-sight velocities.

Given the distance and the location on the sky, this structure is very likely to be the Palca stream, which was also discovered in DES (Shipp et al. 2018). Recent studies by Chang et al. (2020) show that Palca is possibly the extension of Cetus Polar stream found in SDSS (Newberg et al. 2009; Koposov et al. 2012). The kinematic data will help confirm or refute this connection. If it is indeed one stream, this long stream with 6D information will be another critical tool for constraining the Milky Way potential.

We found a total of 25 Palca member stars using the selection criteria defined above, which gives a velocity dispersion of  $\sigma_v = 9.5 \pm 1.8 \text{ km s}^{-1}$  and a systemic velocity of  $v_{\text{hel}} = 98 \pm 2 \text{ km s}^{-1}$  at  $(\alpha, \delta) = (34^{\circ}, -34^{\circ})$ . Based on the large velocity dispersion, the progenitor is very likely to be a dwarf galaxy, which matches with the large stream width observed on the sky. We derived the metallicity of the 11 brightest RGB members of Palca assuming a distance modulus of  $m - M = 17.8$ . These stars have metallicities spanning from  $[\text{Fe}/\text{H}] = -1.5$  to  $[\text{Fe}/\text{H}] = -2.2$ , with a mean metallicity of  $[\text{Fe}/\text{H}] = -2.0$ . However, we were not able to resolve a metallicity dispersion ( $\sigma_{[\text{Fe}/\text{H}]} < 0.16 \text{ dex}$  at 95% confidence). The low metallicity dispersion is likely due to a combination of small sample size and the faintness (and therefore large metallicity uncertainty) of the RGB stars. Although  $S^5$  did not specifically target the Palca

stream, many  $S^5$  fields overlapped with it due to its large width on the sky. We will leave a more thorough analysis of Palca for a future  $S^5$  paper.

## 6. SUMMARY

We present the first spectroscopic measurements on the ATLAS stream and Aliqa Uma stream from  $S^5$  observations, with a total of 96 spectroscopic member stars identified in these two streams (Figure 4 and 5). In combining our spectroscopy with the photometry from DES DR1 and PS1 DR1, and astrometry from *Gaia* DR2, we conclude that the two streams are essentially one stream, despite the discontinuity in the on-sky morphology. We refer to this entire stream as ATLAS-Aliqa Uma stream, or AAU stream. We summarize our main findings here:

- We confirm that in radial velocity, proper motion and heliocentric distance (see Figures 2, 5 and 6) the two streams are seamlessly connected to each other, with a  $\sim 1^{\circ}$  shift in the stream track on the sky at the connection point at  $\phi_1 \sim -12^{\circ}$ ; a feature we call a “kink”. The physical size of the kink feature is  $\sim 0.5 \text{ kpc}$ .
- In addition to the “kink”, we notice a significantly larger stream width on the sky around  $\phi_1 \sim 0^{\circ}$  in the spectroscopic sample (Figure 2 and 5). We call this feature “broadening”. This feature is well detected in a deep photometric map of the stream based on DES DR1 (without spectroscopic or proper motion information). The modeling of the feature reveals that although the linear density of the stream members stays unchanged in this area, the surface brightness of the stream drops by about a factor of two while the stream width gets larger, resulting in two (surface) density gaps at  $\phi_1 \sim -2^{\circ}$  and  $\phi_1 \sim +3^{\circ}$  (Figure 13, 14). This feature is also accompanied by a detectable shift in the stream track (or referred to as “wiggle”) by  $0.2^{\circ}$ . The constant linear density combined with the shift in the stream track strongly supports a perturbation hypothesis as opposed to density variation caused by the epicyclic motion of the stripped stars (Ibata et al. 2020).
- We find that the line-of-sight velocity dispersion varies along the stream. In the Aliqa Uma part (including the “kink”), the velocity dispersion is as large as  $\sim 6 \text{ km s}^{-1}$ , while in the ATLAS part of stream the dispersion is around  $\sim 2 \text{ km s}^{-1}$ . Furthermore, we also see an indication of the velocity gradient at the “kink”, where the line-of-sight velocities show a difference of  $> 20 \text{ km s}^{-1}$  from the

Aliqa Uma part of the stream to the ATLAS part of stream at  $\phi_1 \sim -11^\circ$  (Figure 7). This suggests that the Aliqa Uma component was heavily perturbed in the past, confirming the picture painted based on the discontinuity of the stream on the sky.

- In addition to finding continuity between ATLAS and Aliqa Uma in kinematic space, we observe that they are indistinguishable in metallicity and chemical abundance patterns, further supporting the hypothesis that they are one stream. The mean metallicity of the stream is at  $[\text{Fe}/\text{H}] = -2.2$ , with an unresolved metallicity dispersion ( $< 0.07$  dex at 95% confidence level). The low metallicity dispersion together with the narrow stream width and low velocity dispersion confirm the hypothesis that the progenitor of the stream was likely a globular cluster.
- In the list of high probable member stars identified with help of *Gaia* and DES we notice a possible extension of the Aliqa Uma stream that protrudes out of the stream track around  $\phi_1 \sim -10^\circ$  and  $\phi_2 \sim +2^\circ$  (Figure 11). We call that feature a “spur” as its shape is broadly similar to the feature seen in the GD-1 stream (Price-Whelan & Bonaca 2018). As the  $S^5$  observations did not cover this feature, further spectroscopic observations in this area are needed to confirm or disprove its existence. If this spur feature is real, it extends from the ATLAS stream by  $\sim 2^\circ$  on the sky, or  $\sim 0.9$  kpc which is about a factor of 6 times larger than the separation between the spur and the main stream for GD-1 (Price-Whelan & Bonaca 2018).
- By mapping the probable member stars with proper motion from *Gaia* and photometry from DES DR1 and PS1 DR1, we find that the entire stream covers at least 40 degrees on the sky (Figure 11). As the stream also spans from 20 kpc to 30 kpc in heliocentric distance (Figure 6), the total visible portion of the stream is more than 20 kpc long.
- Using the stream track and spectroscopic sample, we fit a dynamical model to the ATLAS component of the stream in the presence of the LMC and determined that the orbit of the AAU stream has a pericenter of  $13.3^{+0.1}_{-0.2}$  kpc, an apocenter of  $41.0^{+0.4}_{-0.5}$  kpc, an eccentricity of  $0.511 \pm 0.001$ , and an orbital period of  $0.62 \pm 0.01$  Gyr. Using these orbit fits, we also compared the actions of AAU stream with the Milky Way globular clusters and

found that the stream has actions similar to globular clusters that were accreted with the Sagittarius dwarf (Whiting 1, NGC 5824, Pal 12).

- We examine a wide range of baryonic effects on the AAU stream: the Milky Way bar, spiral arms, giant molecular clouds, globular clusters, and dwarf galaxies. Of these, we find that only a nearby passage with the Sagittarius dwarf can create features similar to the observed “kink” between ATLAS and Aliqa Uma. In order to confirm this, a more detailed analysis is needed to fit the perturbed models of the AAU stream to the data and constrain the perturbation (e.g. Erkal & Belokurov 2015a). We also find that the globular cluster NGC 7492 likely has a close passage with AAU and may be able to create features like the “broadening”.
- In addition to the AAU stream, we found another group of stars in the observed fields at a heliocentric velocity of  $\sim 100$  km s $^{-1}$  and a distance of  $\sim 35$  kpc. This structure is unconnected to the AAU stream, and is very likely to be associated with the Palca stream (Figure 1, 19), another stream found in DES and possibly a southern extension of the Cetus Polar Stream.

We want to highlight that the ATLAS and Aliqa Uma streams are the second pair of streams that have been found to be a single, gravitationally perturbed stream. The first example of such a case was the Orphan/Chenab pair found in Koposov et al. (2019). This significant result suggests that 1) many streams that are currently thought to be distinct could in fact have the same progenitor; 2) perturbations at small (for AAU) and large scales (for Orphan/Chenab) play a critical role in the evolution of stellar streams.

The detection of the “kink” and “broadening” features show the power of spectroscopy as part of density variation studies for distant streams. Unlike the GD-1 stream, at a heliocentric distance of 7 – 10 kpc, the AAU stream is three times further away, and therefore *Gaia* proper motion measurements are not available for stream members along the main sequence. Fortunately, the radial velocities provided by the spectroscopic measurements allow us to reliably remove the foreground contamination and present a clean sample of member stars in the streams, making it possible to detect extremely low surface brightness features created by perturbations.

With  $S^5$  we have obtained spectroscopic data on over ten stellar streams (Paper I), some of which present

relatively narrow stream widths, whose progenitors are likely to be globular clusters like the AAU stream. The combination of photometric, astrometric and spectroscopic data will enable crucial new studies of the possible perturbation signatures in these streams.

#### ACKNOWLEDGMENTS

This paper includes data obtained with the Anglo-Australian Telescope in Australia. We acknowledge the traditional owners of the land on which the AAT stands, the Gamilaraay people, and pay our respects to elders past and present. This paper includes data gathered with the 6.5 meter Magellan Telescopes located at Las Campanas Observatory, Chile.

We thank Paul McMillan for providing the posterior MCMC chains of the fit from [McMillan \(2017\)](#).

TSL and APJ are supported by NASA through Hubble Fellowship grant HST-HF2-51439.001 and HST-HF2-51393.001, respectively, awarded by the Space Telescope Science Institute, which is operated by the Association of Universities for Research in Astronomy, Inc., for NASA, under contract NAS5-26555. SK is partially supported by NSF grants AST-1813881, AST-1909584 and Heising-Simons foundation grant 2018-1030. ABP is supported by NSF grant AST-1813881.

This research has made use of the SIMBAD database, operated at CDS, Strasbourg, France ([Wenger et al. 2000](#)), and NASA’s Astrophysics Data System Bibliographic Services.

This paper made use of the Whole Sky Database (wsdb) created by Sergey Koposov and maintained at the Institute of Astronomy, Cambridge by Sergey Koposov, Vasily Belokurov and Wyn Evans with financial support from the Science & Technology Facilities Council (STFC) and the European Research Council (ERC).

This work presents results from the European Space Agency (ESA) space mission Gaia. Gaia data are being processed by the Gaia Data Processing and Analysis Consortium (DPAC). Funding for the DPAC is provided by national institutions, in particular the institutions participating in the Gaia MultiLateral Agreement (MLA). The Gaia mission website is <https://www.cosmos.esa.int/gaia>. The Gaia archive website is <https://archives.esac.esa.int/gaia>.

This project used public archival data from the Dark Energy Survey (DES). Funding for the DES Projects has been provided by the U.S. Department of Energy, the U.S. National Science Foundation, the Ministry of Science and Education of Spain, the Science and Technology Facilities Council of the United Kingdom, the Higher Education Funding Council for England, the Na-

tional Center for Supercomputing Applications at the University of Illinois at Urbana-Champaign, the Kavli Institute of Cosmological Physics at the University of Chicago, the Center for Cosmology and Astro-Particle Physics at the Ohio State University, the Mitchell Institute for Fundamental Physics and Astronomy at Texas A&M University, Financiadora de Estudos e Projetos, Fundação Carlos Chagas Filho de Amparo à Pesquisa do Estado do Rio de Janeiro, Conselho Nacional de Desenvolvimento Científico e Tecnológico and the Ministério da Ciência, Tecnologia e Inovação, the Deutsche Forschungsgemeinschaft, and the Collaborating Institutions in the Dark Energy Survey. The Collaborating Institutions are Argonne National Laboratory, the University of California at Santa Cruz, the University of Cambridge, Centro de Investigaciones Energéticas, Medioambientales y Tecnológicas-Madrid, the University of Chicago, University College London, the DES-Brazil Consortium, the University of Edinburgh, the Eidgenössische Technische Hochschule (ETH) Zürich, Fermi National Accelerator Laboratory, the University of Illinois at Urbana-Champaign, the Institut de Ciències de l’Espai (IEEC/CSIC), the Institut de Física d’Altes Energies, Lawrence Berkeley National Laboratory, the Ludwig-Maximilians Universität München and the associated Excellence Cluster Universe, the University of Michigan, the National Optical Astronomy Observatory, the University of Nottingham, The Ohio State University, the OzDES Membership Consortium, the University of Pennsylvania, the University of Portsmouth, SLAC National Accelerator Laboratory, Stanford University, the University of Sussex, and Texas A&M University. Based in part on observations at Cerro Tololo Inter-American Observatory, National Optical Astronomy Observatory, which is operated by the Association of Universities for Research in Astronomy (AURA) under a cooperative agreement with the National Science Foundation.

The Pan-STARRS1 Surveys (PS1) and the PS1 public science archive have been made possible through contributions by the Institute for Astronomy, the University of Hawaii, the Pan-STARRS Project Office, the Max Planck Society and its participating institutes, the Max Planck Institute for Astronomy, Heidelberg and the Max Planck Institute for Extraterrestrial Physics, Garching, The Johns Hopkins University, Durham University, the University of Edinburgh, the Queen’s University Belfast, the Harvard-Smithsonian Center for Astrophysics, the Las Cumbres Observatory Global Telescope Network Incorporated, the National Central University of Taiwan, the Space Telescope Science Institute, the National Aeronautics and Space Administration under Grant No.

NNX08AR22G issued through the Planetary Science Division of the NASA Science Mission Directorate, the National Science Foundation Grant No. AST-1238877, the University of Maryland, Eotvos Lorand University (ELTE), the Los Alamos National Laboratory, and the Gordon and Betty Moore Foundation.

TSL would like to thank Day for his company during the quarantine while accomplishing this manuscript.

*Facilities:* Anglo-Australian Telescope (AAOmega+2dF); Magellan/Clay (MIKE)

*Software:* `numpy` (van der Walt et al. 2011), `scipy` (Jones et al. 2001), `matplotlib` (Hunter 2007), `astropy` (Astropy Collaboration et al. 2013; Price-Whelan et al. 2018), `emcee` (Foreman-Mackey et al. 2013), `CarPy` (Kelson 2003), `M00G` (Snedden 1973; Sobek et al. 2011), `smhr` (Casey 2014), `q3c` (Koposov & Bartunov 2006), `RVSpecFit` (Koposov 2019) `GPYOpt` (The GPYOpt authors 2016), `STAN` (Carpenter et al. 2017)

## REFERENCES

- Abomalima, A., & Frebel, A. 2018, *ApJS*, 238, 36
- Amorisco, N. C., Gómez, F. A., Vegetti, S., & White, S. D. M. 2016, *MNRAS*, 463, L17
- Astropy Collaboration, Robitaille, T. P., Tollerud, E. J., et al. 2013, *A&A*, 558, A33
- Banik, N., & Bovy, J. 2019, *MNRAS*, 484, 2009
- Bastian, N., & Lardo, C. 2018, *ARA&A*, 56, 83
- Baumgardt, H., Hilker, M., Sollima, A., & Bellini, A. 2019, *MNRAS*, 482, 5138
- Bellazzini, M., Ferraro, F. R., & Ibata, R. 2003, *AJ*, 125, 188
- Belokurov, V., & Koposov, S. E. 2016, *MNRAS*, 456, 602
- Belokurov, V., Zucker, D. B., Evans, N. W., et al. 2006, *ApJ*, 642, L137
- . 2007, *ApJ*, 654, 897
- Bernard, E. J., Ferguson, A. M. N., Schlafly, E. F., et al. 2016, *MNRAS*, 463, 1759
- Bernstein, R., Shtetman, S. A., Gunnels, S. M., Mochnacki, S., & Athey, A. E. 2003, in *Society of Photo-Optical Instrumentation Engineers (SPIE) Conference Series*, Vol. 4841, *Instrument Design and Performance for Optical/Infrared Ground-based Telescopes*, ed. M. Iye & A. F. M. Moorwood, 1694–1704
- Betancourt, M. 2017, arXiv e-prints, arXiv:1701.02434
- Bonaca, A., Conroy, C., Price-Whelan, A. M., & Hogg, D. W. 2019a, *ApJ*, 881, L37
- Bonaca, A., Hogg, D. W., Price-Whelan, A. M., & Conroy, C. 2019b, *ApJ*, 880, 38
- Bonaca, A., Pearson, S., Price-Whelan, A. M., et al. 2020, *ApJ*, 889, 70
- Bovy, J. 2016, *Phys. Rev. Lett.*, 116, 121301
- Bovy, J., Erkal, D., & Sanders, J. L. 2017, *MNRAS*, 466, 628
- Bovy, J., Leung, H. W., Hunt, J. A. S., et al. 2019, *MNRAS*, 490, 4740
- Bressan, A., Marigo, P., Girardi, L., et al. 2012, *MNRAS*, 427, 127
- Buckley, M. R., & Peter, A. H. G. 2018, *Phys. Rep.*, 761, 1
- Bullock, J. S., Kravtsov, A. V., & Weinberg, D. H. 2001, *ApJ*, 548, 33
- Caldwell, N., Bonaca, A., Price-Whelan, A., Sesar, B., & Walker, M. 2020, arXiv e-prints, arXiv:2004.14350
- Carlberg, R. G. 2012, *ApJ*, 748, 20
- . 2020, *ApJ*, 889, 107
- Carlberg, R. G., & Grillmair, C. J. 2013, *ApJ*, 768, 171
- Carpenter, B., Gelman, A., Hoffman, M., et al. 2017, *Journal of Statistical Software, Articles*, 76, 1. <https://www.jstatsoft.org/v076/i01>
- Carraro, G., Zinn, R., & Moni Bidin, C. 2007, *A&A*, 466, 181
- Carrera, R., Pancino, E., Gallart, C., & del Pino, A. 2013, *MNRAS*, 434, 1681
- Carretta, E., Bragaglia, A., Gratton, R. G., et al. 2014, *A&A*, 561, A87
- Casey, A. R. 2014, PhD thesis, Australian National University
- Chambers, K. C., Magnier, E. A., Metcalfe, N., et al. 2016, arXiv e-prints, arXiv:1612.05560
- Chang, J., Yuan, Z., Xue, X.-X., et al. 2020, arXiv e-prints, arXiv:2003.02378
- Choi, J., Dotter, A., Conroy, C., et al. 2016, *ApJ*, 823, 102
- Clem, J. L. 2006, PhD thesis, University of Victoria, Canada
- Combes, F., Leon, S., & Meylan, G. 1999, *A&A*, 352, 149
- Cox, D. P., & Gómez, G. C. 2002, *ApJS*, 142, 261
- de Boer, T. J. L., Belokurov, V., Koposov, S. E., et al. 2018, *MNRAS*, 477, 1893
- de Boer, T. J. L., Erkal, D., & Gieles, M. 2019, arXiv e-prints, arXiv:1911.05745
- Deason, A. J., Belokurov, V., & Evans, N. W. 2011, *MNRAS*, 416, 2903
- Dehnen, W., & Binney, J. 1998, *MNRAS*, 294, 429
- Dehnen, W., Odenkirchen, M., Grebel, E. K., & Rix, H.-W. 2004, *AJ*, 127, 2753
- DES Collaboration. 2016, *MNRAS*, 460, 1270



- DES Collaboration, Abbott, T. M. C., Abdalla, F. B., et al. 2018, *ApJS*, 239, 18
- Desai, S., Armstrong, R., Mohr, J. J., et al. 2012, *ApJ*, 757, 83
- Diemand, J., Moore, B., & Stadel, J. 2005, *Nature*, 433, 389
- Dotter, A. 2016, *ApJS*, 222, 8
- Dotter, A., Chaboyer, B., Jevremović, D., et al. 2008, *ApJS*, 178, 89
- Erkal, D., & Belokurov, V. 2015a, *MNRAS*, 454, 3542
- . 2015b, *MNRAS*, 450, 1136
- Erkal, D., Koposov, S. E., & Belokurov, V. 2017, *MNRAS*, 470, 60
- Erkal, D., Sanders, J. L., & Belokurov, V. 2016, *MNRAS*, 461, 1590
- Erkal, D., Belokurov, V., Laporte, C. F. P., et al. 2019, *MNRAS*, 487, 2685
- Fardal, M. A., van der Marel, R. P., Sohn, S. T., & del Pino Molina, A. 2019, *MNRAS*, 486, 936
- Foreman-Mackey, D., Hogg, D. W., Lang, D., & Goodman, J. 2013, *PASP*, 125, 306
- Gaia Collaboration, Brown, A. G. A., Vallenari, A., et al. 2018a, *A&A*, 616, A1
- Gaia Collaboration, Babusiaux, C., van Leeuwen, F., et al. 2018b, *A&A*, 616, A10
- Gaia Collaboration, Helmi, A., van Leeuwen, F., et al. 2018c, *A&A*, 616, A12
- Gelman, A., Carlin, J. B., Stern, H. S., et al. 2013, *Bayesian data analysis* (CRC press)
- Gelman, A., & Rubin, D. B. 1992, *Statist. Sci.*, 7, 457. <https://doi.org/10.1214/ss/1177011136>
- Gibbons, S. L. J., Belokurov, V., & Evans, N. W. 2014, *MNRAS*, 445, 3788
- . 2017, *MNRAS*, 464, 794
- Gonzalez, J., Dai, Z., Hennig, P., & Lawrence, N. 2016, in *Proceedings of Machine Learning Research*, Vol. 51, *Proceedings of the 19th International Conference on Artificial Intelligence and Statistics*, ed. A. Gretton & C. C. Robert (Cadiz, Spain: PMLR), 648–657. <http://proceedings.mlr.press/v51/gonzalez16a.html>
- Gravity Collaboration, Abuter, R., Amorim, A., et al. 2019, *A&A*, 625, L10
- Green, A. M., Hofmann, S., & Schwarz, D. J. 2004, *MNRAS*, 353, L23
- Grillmair, C. J., & Carlin, J. L. 2016, in *Astrophysics and Space Science Library*, Vol. 420, *Tidal Streams in the Local Group and Beyond*, ed. H. J. Newberg & J. L. Carlin, 87
- Grillmair, C. J., & Dionatos, O. 2006, *ApJ*, 643, L17
- Harris, W. E. 2010, *ArXiv e-prints*, arXiv:1012.3224
- Hattori, K., Erkal, D., & Sanders, J. L. 2016, *MNRAS*, 460, 497
- Hernquist, L. 1990, *ApJ*, 356, 359
- Hoffman, M. D., & Gelman, A. 2011, *arXiv e-prints*, arXiv:1111.4246
- Hofmann, S., Schwarz, D. J., & Stoecker, H. 2001, *Phys. Rev. D*, 64, 083507
- Hu, W., Barkana, R., & Gruzinov, A. 2000, *Phys. Rev. Lett.*, 85, 1158
- Hui, L., Ostriker, J. P., Tremaine, S., & Witten, E. 2017, *Phys. Rev. D*, 95, 043541
- Hunter, J. D. 2007, *Computing in Science & Engineering*, 9, 90. <http://scitation.aip.org/content/aip/journal/cise/9/3/10.1109/MCSE.2007.55>
- Husser, T. O., Wende-von Berg, S., Dreizler, S., et al. 2013, *A&A*, 553, A6
- Ibata, R., Thomas, G., Famaey, B., et al. 2020, *arXiv e-prints*, arXiv:2002.01488
- Ibata, R. A., Malhan, K., & Martin, N. F. 2019, *ApJ*, 872, 152
- Irwin, M. 1999, in *IAU Symposium*, Vol. 192, *The Stellar Content of Local Group Galaxies*, ed. P. Whitelock & R. Cannon, 409
- Jethwa, P., Erkal, D., & Belokurov, V. 2018, *MNRAS*, 473, 2060
- Johnston, K. V., Spergel, D. N., & Haydn, C. 2002, *ApJ*, 570, 656
- Jones, E., Oliphant, T., Peterson, P., et al. 2001, *SciPy: Open source scientific tools for Python*, . <http://www.scipy.org/>
- Kallivayalil, N., van der Marel, R. P., Besla, G., Anderson, J., & Alcock, C. 2013, *ApJ*, 764, 161
- Kelson, D. D. 2003, *PASP*, 115, 688
- Kim, S. Y., Peter, A. H. G., & Hargis, J. R. 2018, *Phys. Rev. Lett.*, 121, 211302
- Koposov, S., & Bartunov, O. 2006, in *Astronomical Society of the Pacific Conference Series*, Vol. 351, *Astronomical Data Analysis Software and Systems XV*, ed. C. Gabriel, C. Arviset, D. Ponz, & S. Enrique, 735
- Koposov, S. E. 2019, *RVSPECFIT: Radial velocity and stellar atmospheric parameter fitting*, , ascl:1907.013
- Koposov, S. E., Belokurov, V., & Evans, N. W. 2013, *ApJ*, 766, 79
- Koposov, S. E., Belokurov, V., Torrealba, G., & Evans, N. W. 2015, *ApJ*, 805, 130
- Koposov, S. E., Irwin, M., Belokurov, V., et al. 2014, *MNRAS*, 442, L85
- Koposov, S. E., Rix, H.-W., & Hogg, D. W. 2010, *ApJ*, 712, 260

- Koposov, S. E., Yoo, J., Rix, H.-W., et al. 2009, *ApJ*, 696, 2179
- Koposov, S. E., Gilmore, G., Walker, M. G., et al. 2011, *ApJ*, 736, 146
- Koposov, S. E., Belokurov, V., Evans, N. W., et al. 2012, *ApJ*, 750, 80
- Koposov, S. E., Belokurov, V., Li, T. S., et al. 2019, *MNRAS*, 485, 4726
- Kruijssen, J. M. D., Pfeffer, J. L., Chevance, M., et al. 2020, arXiv e-prints, arXiv:2003.01119
- Küpper, A. H. W., Kroupa, P., Baumgardt, H., & Heggie, D. C. 2010, *MNRAS*, 401, 105
- Kuzma, P. B., Da Costa, G. S., Keller, S. C., & Maunder, E. 2015, *MNRAS*, 446, 3297
- Law, D. R., & Majewski, S. R. 2010, *ApJ*, 714, 229
- Li, T. S., Simon, J. D., Drlica-Wagner, A., et al. 2017, *ApJ*, 838, 8
- Li, T. S., Simon, J. D., Kuehn, K., et al. 2018, ArXiv e-prints, arXiv:1804.07761
- Li, T. S., Koposov, S. E., Zucker, D. B., et al. 2019, *MNRAS*, 490, 3508
- Long, K., & Murali, C. 1992, *ApJ*, 397, 44
- Malhan, K., Ibata, R. A., Carlberg, R. G., Valluri, M., & Freese, K. 2019, *ApJ*, 881, 106
- Malhan, K., Ibata, R. A., & Martin, N. F. 2018, *MNRAS*, 481, 3442
- Massari, D., Koppelman, H. H., & Helmi, A. 2019, *A&A*, 630, L4
- McConnachie, A. W. 2012, *AJ*, 144, 4
- McMillan, P. J. 2017, *MNRAS*, 465, 76
- Miville-Deschênes, M.-A., Murray, N., & Lee, E. J. 2017, *ApJ*, 834, 57
- Monari, G., Famaey, B., Siebert, A., et al. 2016, *MNRAS*, 461, 3835
- Muraveva, T., Delgado, H. E., Clementini, G., Sarro, L. M., & Garofalo, A. 2018, *MNRAS*, 481, 1195
- Nadler, E. O., Banerjee, A., Adhikari, S., Mao, Y.-Y., & Wechsler, R. H. 2020, arXiv e-prints, arXiv:2001.08754
- Nadler, E. O., Gluscevic, V., Boddy, K. K., & Wechsler, R. H. 2019, *ApJ*, 878, L32
- Neal, R. M. 2012, arXiv e-prints, arXiv:1206.1901
- Newberg, H. J., Yanny, B., & Willett, B. A. 2009, *ApJ*, 700, L61
- Newton, O., Cautun, M., Jenkins, A., Frenk, C. S., & Helly, J. C. 2018, *MNRAS*, 479, 2853
- Odenkirchen, M., Grebel, E. K., Rockosi, C. M., et al. 2001, *ApJ*, 548, L165
- Pawlowski, M. S., & Kroupa, P. 2014, *ApJ*, 790, 74
- Pearson, S., Price-Whelan, A. M., & Johnston, K. V. 2017, *Nature Astronomy*, 1, 633
- Piatek, S., Pryor, C., & Olszewski, E. W. 2016, *AJ*, 152, 166
- Pietrzyński, G., Graczyk, D., Gieren, W., et al. 2013, *Nature*, 495, 76
- Plummer, H. C. 1911, *MNRAS*, 71, 460
- Portail, M., Gerhard, O., Wegg, C., & Ness, M. 2017, *MNRAS*, 465, 1621
- Price-Whelan, A. M., & Bonaca, A. 2018, *ApJ*, 863, L20
- Price-Whelan, A. M., Mateu, C., Iorio, G., et al. 2019, *AJ*, 158, 223
- Price-Whelan, A. M., Sesar, B., Johnston, K. V., & Rix, H.-W. 2016, *ApJ*, 824, 104
- Price-Whelan, A. M., Sipőcz, B. M., Günther, H. M., et al. 2018, *AJ*, 156, 123
- Reid, M. J., & Brunthaler, A. 2004, *ApJ*, 616, 872
- Riley, A. H., & Strigari, L. E. 2020, *MNRAS*, 494, 983
- Rockosi, C. M., Odenkirchen, M., Grebel, E. K., et al. 2002, *AJ*, 124, 349
- Sanders, J. L., Smith, L., & Evans, N. W. 2019, *MNRAS*, 488, 4552
- Schlegel, D. J., Finkbeiner, D. P., & Davis, M. 1998, *ApJ*, 500, 525
- Schönrich, R., Binney, J., & Dehnen, W. 2010, *MNRAS*, 403, 1829
- Shanks, T., Metcalfe, N., Chehade, B., et al. 2015, *MNRAS*, 451, 4238
- Shipp, N., Drlica-Wagner, A., Balbinot, E., et al. 2018, *ApJ*, 862, 114
- Shipp, N., Li, T. S., Pace, A. B., et al. 2019, *ApJ*, 885, 3
- Siegal-Gaskins, J. M., & Valluri, M. 2008, *ApJ*, 681, 40
- Snedden, C. A. 1973, PhD thesis, THE UNIVERSITY OF TEXAS AT AUSTIN.
- Sobeck, J. S., Kraft, R. P., Sneden, C., et al. 2011, *AJ*, 141, 175
- Sohn, S. T., Besla, G., van der Marel, R. P., et al. 2013, *ApJ*, 768, 139
- Springel, V., Wang, J., Vogelsberger, M., et al. 2008, *MNRAS*, 391, 1685
- The GPYOpt authors. 2016, GPYOpt: A Bayesian Optimization framework in Python, <http://github.com/SheffieldML/GPYOpt>, ,
- van der Marel, R. P., Alves, D. R., Hardy, E., & Suntzeff, N. B. 2002, *AJ*, 124, 2639
- van der Marel, R. P., & Kallivayalil, N. 2014, *ApJ*, 781, 121
- van der Walt, S., Colbert, S. C., & Varoquaux, G. 2011, *Computing in Science & Engineering*, 13, 22. <http://scitation.aip.org/content/aip/journal/cise/13/2/10.1109/MCSE.2011.37>
- Vasiliev, E. 2019a, *MNRAS*, 484, 2832
- . 2019b, *MNRAS*, 482, 1525

- Walker, M. G., Mateo, M., Olszewski, E. W., et al. 2006, AJ, 131, 2114
- Webb, J. J., & Bovy, J. 2019, MNRAS, 485, 5929
- Wegg, C., Gerhard, O., & Portail, M. 2015, MNRAS, 450, 4050
- Wenger, M., Ochsenbein, F., Egret, D., et al. 2000, A&AS, 143, 9
- Yoon, J. H., Johnston, K. V., & Hogg, D. W. 2011, ApJ, 731, 58

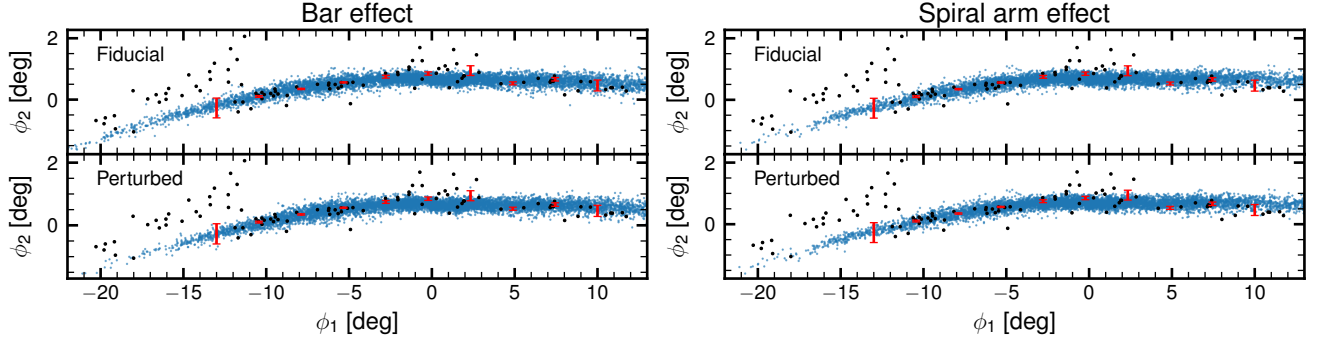


**Figure 20.** Example of perturbations from bar (left) and spiral arms (right) which produce the largest change in the stream track. *Left panels* show the effect of the Milky Way bar. The top panel shows the fiducial bar simulation with a pattern speed of  $\Omega = 1000 \text{ km s}^{-1} \text{ kpc}^{-1}$  and the bottom panel shows the perturbed stream evolved in the presence of a bar with pattern speed  $\Omega = 42.3 \text{ km s}^{-1} \text{ kpc}^{-1}$ . The maximum deviation is  $0.1^\circ$ . *Right panels* show the effect of spiral arms on ATLAS. The top panel shows the fiducial spiral arm simulation with a pattern speed of  $\Omega = 1000 \text{ km s}^{-1} \text{ kpc}^{-1}$  while the bottom panel shows the simulation with the largest track deviation with a pattern speed of  $\Omega = 26.6 \text{ km s}^{-1} \text{ kpc}^{-1}$ . The largest deviation in the track is  $0.02^\circ$  showing that the spiral cannot create any appreciable features in ATLAS.

## APPENDIX

### A. COORDINATE TRANSFORMATION MATRIX

The transformation from celestial coordinates  $(\alpha, \delta)$  to the stream coordinates  $(\phi_1, \phi_2)$  is given by (Shipp et al. 2019):

$$\begin{bmatrix} \cos(\phi_1) \cos(\phi_2) \\ \sin(\phi_1) \cos(\phi_2) \\ \sin(\phi_2) \end{bmatrix} = \begin{bmatrix} 0.83697865 & 0.29481904 & -0.4610298 \\ 0.51616778 & -0.70514011 & 0.4861566 \\ 0.18176238 & 0.64487142 & 0.74236331 \end{bmatrix} \times \begin{bmatrix} \cos(\alpha) \cos(\delta) \\ \sin(\alpha) \cos(\delta) \\ \sin(\delta) \end{bmatrix}$$

### B. EXAMPLE OF BAR AND SPIRAL ARM PERTURBATIONS

In Section 5.2.1, 5.2.3 we considered the effect of the Milky Way bar and spiral arm respectively. Both of these can create only modest perturbations in the stream. In Figure 20 we show the stream realizations with the largest changes in the stream track ( $0.1^\circ$  for the bar and  $0.02^\circ$  for the spiral arms).

### C. EXAMPLE OF GLOBULAR CLUSTER PERTURBATIONS

In Section 5.2.5 we explored the effect of globular clusters on the AAU stream. Of these, NGC 7492 has the closest approach to AAU with a median approach distance of 0.55 kpc. In Figure 21 we show five examples perturbations from NGC 7492. While none of these create kinks as large as the one between ATLAS and Aliqa Uma, several perturbations create smaller wiggles in the stream as well as broadening of the stream width qualitatively consistent with the observed wiggle and broadening at  $\phi_1 \sim 3^\circ$ .



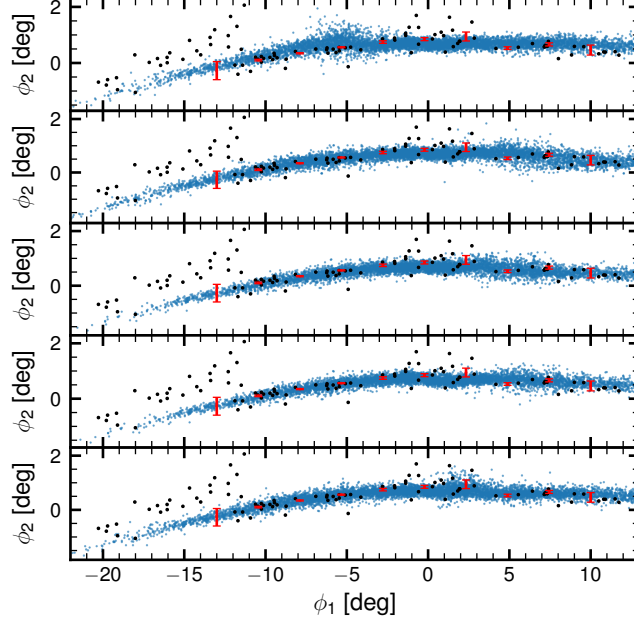


**Figure 21.** Example of perturbations from NGC 7492 to the AAU stream. We show five perturbations out of the 100 sampled in Section 5.2.5. These were chosen due to the change in the stream track as well as the broadening in the stream width. The top panel shows the perturbation with the largest change in the stream track, producing a kink with a size of  $0.19^\circ$  at  $\phi_1 \sim -5^\circ$  and an associated broadening of the stream. This is qualitatively similar to the wiggle and broadening observed at  $\phi_1 \sim 3^\circ$ .

**Table 1.** Spectroscopic Members in ATLAS Stream and Aliqa Uma Stream. Only first few lines are shown here. Full table is available in the online version in machine readable format.

<i>Gaia</i> DR2 Source ID	RA (deg)	Decl. (deg)	SNR	<i>G</i> (mag)	$v_{\text{hel}}$ ( $\text{km s}^{-1}$ )	$\sigma_v$ ( $\text{km s}^{-1}$ )	[Fe/H]	$\sigma_{[\text{Fe}/\text{H}]}$
2362404846580059648	9.109642	-20.418631	21.2	16.48	-148.16	2.91		
2362395599515154816	9.387846	-20.461972	3.7	19.56	-142.35	7.34		
2350314513642106624	9.890383	-20.839192	17.9	17.72	-148.30	1.28	-2.28	0.26
2350310424833246592	9.974475	-20.892894	32.5	16.83	-156.83	0.90		
2350245137034340864	10.193825	-21.129194	7.2	18.26	-147.61	3.77		
2350348972163836160	11.151796	-21.480250	36.5	16.55	-144.90	0.80	-2.17	0.15
2349548630777593344	11.609142	-22.164725	8.8	18.50	-141.97	2.20	-2.35	0.53
2349572579516107264	11.654787	-21.817247	4.9	18.99	-142.44	5.29		
2349268564550587904	12.229042	-22.749461	22.9	16.38	-134.19	1.02	-2.58	0.19